

1           [Click here to take you to the GEOCARB .NET downloading page](#)

2

### 3   User-friendly Carbon-Cycle Modelling and Aspects of Phanerozoic Climate Change

4   Trond H. Torsvik<sup>1,2</sup>, Dana L. Royer<sup>3</sup>, Chloé M. Marcilly<sup>1</sup>, Stephanie C. Werner<sup>1</sup>

5   <sup>1</sup>Centre for Planetary Habitability (PHAB), University of Oslo, 0315 Oslo, Norway

6   <sup>2</sup>School of Geosciences, University of Witwatersrand, Johannesburg 2050, South Africa

7   <sup>3</sup>Department of Earth and Environmental Sciences, Wesleyan University, Middletown, Connecticut 06459, USA.

8

## 9   ABSTRACT

10   [TO BE FINALYZED after all comments](#)

14   *Keywords:* Carbon-cycle modelling, Paleogeography, CO<sub>2</sub> sources and sinks, Phanerozoic

16   

## 1. Introduction

17   Greenhouse gases trap heat in the Earth's atmosphere and warm our planet. On geological time-  
18 scales CO<sub>2</sub> is considered the most influential greenhouse gas in modulating atmospheric temperature,  
19 while other potent greenhouse gases (e.g., H<sub>2</sub>O and CH<sub>4</sub>) have atmospheric residence times only on the  
20 order of days-to-years. Judged from the sedimentary glacial record it appears that our planet has mostly  
21 been hotter than today and too warm to sustain continental-scale glaciations. Ice-free intervals are  
22 explained by high greenhouse gas concentration and temperatures, and termed greenhouse climates.

23   The Phanerozoic represents the last 540 Myrs million years ([Fig. 1](#)) and is dominated by a  
24 greenhouse climate (80%) but were interrupted by three major periods of cold glacial conditions in the  
25 end-Ordovician (~445 Ma; [Cocks & Torsvik 2021](#)), Permo-Carboniferous (~330-260 Ma; [Montañez &](#)  
26 [Poulsen 2013](#)) and the second half of the Cenozoic ([DeConto & Pollard 2003](#); [Ruggieri et al. 2009](#); [De](#)  
27 [Schepper et al. 2014](#); [Bierman et al. 2014](#)). These icehouse phases, characterized by on average lower  
28 temperatures and CO<sub>2</sub> concentrations, are named the Hirnantian, the Late Paleozoic Ice Age (LPIA)  
29 and the End-Cenozoic Ice Age (ECIA). A modern CO<sub>2</sub> threshold for continental-scale glacial inception  
30 is ~500 ppm ([Royer 2006](#)), but with a fainter sun, the glacial inception thresholds during the Hirnantian  
31 and LPIA would be close to 1000 and 850 ppm, respectively ([Fig. 1](#)). This assumes a climate sensitivity  
32 of ~6°C per doubling of CO<sub>2</sub> with land ice ([Royer 2006](#)).

33   CO<sub>2</sub> concentrations (nor temperatures) cannot be measured in deep time, and we therefore must  
34 rely on models or proxies ([Section 7](#)). For the past 450 million years, CO<sub>2</sub> proxies during greenhouse  
35 climates average ~1100 ppm whilst the Phanerozoic icehouse intervals average ~480 ppm. But a proxy-  
36 based picture of CO<sub>2</sub> concentrations before 450 Ma is lacking and thus CO<sub>2</sub> levels for most of Earth's  
37 history must be estimated from carbon-cycle models. Models are also useful to test what processes  
38 (sources and sinks; [Section 3](#)) can explain variations in atmospheric CO<sub>2</sub>. Models can be loosely

39 classified as inverse (GEOCARB: Berner, 2004; 2006 and modern variations reviewed in Royer *et al.*  
 40 2014) or forward (e.g., COPSE, GEOCLIM, SCION: Lenton *et al.* 2018; Godderis *et al.* 2014; Mills et  
 41 al. 2021), depending on whether isotopic proxy data (e.g.,  $\delta^{13}\text{C}$ ) are *parametrized* (input time-series) or  
 42 *predicted* from the model, respectively. Both model types, however, incorporate several biological and  
 43 geological/tectonic forcing parameters (time-series) that should be similar in all models.

44 Carbon-cycle models suggest very high atmospheric CO<sub>2</sub> levels at the dawn of the Phanerozoic  
 45 (Fig. 1), but model predictions differ by more than 4000 ppm and model-proxy differences during the  
 46 end-Ordovician (Hirnantian glaciation) can be more than 5000 ppm. From proxies, a systematic decline  
 47 in CO<sub>2</sub> levels in the mid-late Paleozoic (410-340 Ma) is commonly linked to the idea of CO<sub>2</sub> absorption  
 48 by a massive increase of terrestrial plants and the advent of large trees during the Devonian (Berner  
 49 1998). Such declining CO<sub>2</sub> levels is also predicted from models but (e.g.) reconstructed CO<sub>2</sub> levels from  
 50 the SCION model (Mills *et al.* 2021) are consistently higher than CO<sub>2</sub> proxy estimates (Fig. 1).  
 51 Atmospheric CO<sub>2</sub> from proxies and the GEOCARB model (Royer *et al.* 2014) are consistently low  
 52 during the LPIA whilst other models generally predict higher CO<sub>2</sub> levels. Conversely, the GEOCARB  
 53 model predict very low CO<sub>2</sub> ‘icehouse’ levels for the past 200 Myrs. None of the models (Fig. 1) capture  
 54 low CO<sub>2</sub> concentrations during the Hirnantian glacial event.

55 Many of the relatively large, modelled differences in atmospheric CO<sub>2</sub> are arguably caused by  
 56 differences in time-dependent parametrization of plate tectonic degassing and silicate weathering  
 57 (Section 3), and benchmarking of carbon-cycle models are urgently required. In this contribution we  
 58 focus on carbon-cycle modelling with a user-friendly version of *GEOCARB*, hereafter dubbed  
 59 *GEOCARB\_NET*. We notably highlight how certain key input parameters can seriously affect  
 60 reconstructed CO<sub>2</sub> levels and how models and proxies can better be reconciled. Detailed instructions  
 61 how to produce the many diagrams in this paper are detailed in a supplementary file.

## 62 2. Technical and operational issues in brief

63 *GEOCARB\_NET* is a windows-based graphical user interface (GUI) for the geologic carbon and sulfur  
 64 cycle model *GEOCARB*, originally developed by Berner (1991). The GEOCARB model has been  
 65 updated many times and the GUI developed here (GEOCARB\_NET2023, Fig. 2a) is based on the  
 66 *GEOCARBSULFvolc* model (Berner 2006a, b), and specifically an R-code written by Dana Royer and  
 67 first reported in Royer *et al.* (2014). The original R-code is here named GEOCARB\_2022.R but the  
 68 GUI occasionally rewrite the R-code and always produces a version named ‘*GEOCARB\_LastRun.R*’,  
 69 which is run by the GUI.

70 The GEOCARB\_NET start-up page has four menus (‘Organize’, ‘Edit’, ‘Maps’ and ‘Help’, Fig.  
 71 3a), five panels that controls model calculations and libraries, and the two graphical display panels. The  
 72 graphical displays are empty at start-up, but by clicking ‘Run Model’ (left-hand panel, Fig. 3b) your  
 73 latest model will run and show estimated atmospheric CO<sub>2</sub> ( $p\text{CO}_2$ ) and  $p\text{O}_2$  levels in the lower and  
 74 upper graphical panel, respectively. If GEOCARB\_NET is used for the first time, the default model is

75 that of [Marcilly et al. \(2021, M12\)](#) but other published models and refined versions of the [Marcilly et](#)  
 76 [al. \(2021\)](#) models can be found in ‘*Restore System*’ in the ‘*Organize*’ menu ([Fig. 3a](#)). The ‘*Latest Model*  
 77 (*M12*)’ is that of [Marcilly et al. \(2021, M12\)](#) with refined silicate weathering parametrization for the  
 78 past 540 Myrs.

## 79 **2.1 Input files**

80 Running a model (*‘Run Model’*) requires two input files. One of these is named  
 81 ‘*GEOCARB\_input\_arrays.CSV*’ and contains the values and error bounds for twelve different time-  
 82 series ([Fig. 2b](#)). These are listed in 10 Myr intervals back to 570 Ma. A second file,  
 83 ‘*GEOCARB\_input\_summaries.CSV*’ provides a summary of all the input parameters and the  
 84 parameterization of 57 time-invariant constants. The input file structures (in Excel format) follow [Royer](#)  
 85 [et al. \(2014\)](#) ([Appendix 1](#)) who introduced new formulations for land area ( $f_A$ ), fraction of land area  
 86 undergoing chemical weathering ( $f_{AW}/f_A$ ), runoff ( $f_D$ ), and continental temperature (*GEOG*). The old  
 87 ([Berner 2006a, b](#)) and revised values (parameters ending with ‘*Godderis*’) are provided in the  
 88 ‘*GEOCARB\_input\_arrays*’ but in *GEOCARB\_NET* the non-Goddéris parameter choices ([‘Berner’](#)) are  
 89 not used (“*Godderis*” is set to TRUE in ‘*GEOCARB\_LastRun.R*’). In the GUI, parameters ending with  
 90 ‘*Godderis*’ has also been abbreviated to ‘*G*’ ([Fig. 2b](#)) and non-Goddéris parameter choices are not  
 91 displayed in ‘*Time-series*’ in the ‘*Edit*’ menu ([Fig. 3a](#)). The ‘*tectonic*’ parameters  $f_{A\_G}$  and  $f_{AW}/f_{A\_G}$   
 92 were refined in [Marcilly et al. \(2021\)](#) for the past 520 Myrs, and they also updated  $f_{SR}$  (seafloor creation  
 93 rate relative present day) back to 570 Ma.

## 94 **2.2 Output file**

95 ‘*Run Model*’ ([Fig. 3b](#)) calculates  $pCO_2$  and  $pO_2$  based on the parametrization in the two input files  
 96 described above. The data are not only displayed in the two graphic panels, but the system also generates  
 97 an output file named *GEOCARB\_Output.csv*, which comes in two different formats, depending on if  
 98 *GEOCARB\_NET* is run with and without ‘*Error Analysis*’ ([Fig. 2c](#)). Input and output files are in the  
 99 main directory (c:/*Geocarb\_NET*) and the ‘*GEOCARB\_output.CSV*’ file can be opened directly in  
 100 *GEOCARB\_NET* (sub-option ‘*Open GEOCARB\_OUTPUT in EXCEL*’; [Fig. 3a](#)).

## 101 **2.3 Library files**

102 *GEOCARB\_NET* also include original input files for some published *GEOCARB* models, which  
 103 can be found in the ‘*Library*’ folder ([Fig. 2a](#)) and library models are selected in ‘*Restore System*’ in the  
 104 ‘*Organize*’ menu ([Fig. 3a](#)). Technically speaking, ‘*Restore System*’ copies the original input files  
 105 ‘*GEOCARB\_input\_arrays*’ and ‘*GEOCARB\_input\_summaries*’ from the ‘*Library*’ sub-folder (e.g.,  
 106 /*Library/M12* for Model 12 of [Marcilly et al. 2021](#)) to the main folder (c:/*Geocarb\_Net*),  
 107 ‘*GEOCARB\_LastRun.R*’ is executed and then display the data in the GUI ([Fig. 2a](#)). [Figure 3b](#) shows an  
 108 example of what the GUI will look like when Model 12 of [Marcilly et al. \(2021\)](#) is run with the ‘*Error*  
 109 *analysis*’ and ‘*Hirnantian Glaciation*’ options.

110 The lower panel shows atmospheric CO<sub>2</sub> levels from models or proxies whilst the upper panel, by  
 111 default, shows modelled oxygen, but in our example (Fig. 3b), we have here selected ‘Plot Temperature’  
 112 in the ‘chart settings’ panel. We have implemented two temperature compilations, ‘tropical’ sea surface  
 113 temperatures (SSTs) and global average temperatures (GATs; Scotese *et al.* 2021) for the past 520 and  
 114 540 Ma, respectively (Section 7). Temperature data are found in the file “SST\_5Ma\_Binns\_Latitude  
 115 0\_30 and GAT\_Scotese2021\_5Ma\_Intervals.csv”, which is located in the /Temperature folder (Fig. 2a).  
 116 The SST curve is a running mean curve (5 Myr bins) and listed with 1 $\sigma$  errors. The mean GAT curve is  
 117 estimated from the size of past climate belts, broadly like the SSTs for the past 400 Myrs, but in the  
 118 Early Paleozoic they differ significantly (Fig. 3b).

119 In Figure 3b we also display individual CO<sub>2</sub> proxies included in GEOCARB\_NET (Section 7), and  
 120 which can be found in the file ‘Royer2018\_VC\_PP\_Raw\_CO2.csv’ (sub-directory /Proxies). Selection  
 121 of individual proxies or mean proxy curves to plot are controlled in the ‘Proxies’ panel.

## 122 2.4 Error analysis

123 A Monte Carlo error analysis, introduced in Royer *et al.* (2014), was originally implemented in  
 124 GEOCARB\_NET but due to a complex process of reducing initially prescribed variances to avoid  
 125 model failure we opted for a simpler error analysis where 14 important time-series and constants are  
 126 assigned a percentage error (Fig. 4). Applying a percentage error of 4% closely reproduce Monte Carlo  
 127 Estimates (Fig. 4a; ‘inner bands’; Royer *et al.* 2014). If GEOCARB\_NET is run with ‘Error Analysis’,  
 128 the program reports CO<sub>2</sub> levels with a lower and upper bound (Fig. 2c). Increasing the percentage error  
 129 to more than 10% (Fig. 4a) will commonly result in model failure. When the model is run with ‘Error  
 130 Analysis’ then the ERROR (%) column in ‘GEOCARB\_Output’ represent the cumulative error in  
 131 estimated CO<sub>2</sub>. By default, all the boxes in Fig. 4b are ticked on to be included in the error analysis but  
 132 the operator can also select specific parameters to investigate their sensitivity to the error setting.

## 133 3. Plate tectonic CO<sub>2</sub> sources and sinks

134 Plate tectonics controls the distribution of continents and oceans, construction of mountains, arc-  
 135 volcanism, topography, and weathering (Fig. 5), and plays a key role in regulating atmospheric  
 136 greenhouse gas concentrations via *sources* (volcanic emissions and metamorphic decarbonation in  
 137 continental arcs) and *sinks* (silicate weathering and carbon burial) (Walker *et al.* 1981; Berner *et al.*  
 138 1983; Marshall *et al.* 1988; Otto-Bliesner 1995; Raymo *et al.* 1988; Gibbs *et al.* 1999; Berner 2004;  
 139 Goddériss *et al.* 2014; Marcilly *et al.* 2021). Earth is singular amongst the rocky planets in the Solar  
 140 System in having plate tectonics and subduction enables recycling of volatile elements between the  
 141 surface and the mantle. But when modern plate tectonics started is debated and range from the Hadean  
 142 (> 4 Ga) to the Neoproterozoic (~700 Ma, Stern 2018).

### 143 3.1 Changing CO<sub>2</sub> Sourcing

The degassing parameterization in GEOCARB\_NET is expressed as a time-dependent rate relative to present-day ( $f_{SR}$ ), originally defined as the *seafloor creation rate*, which can be calculated with sufficient confidence for the last 83 Myrs from oceanic lithospheric age-grids estimated from magnetic anomalies. Before that time, this approach has much larger uncertainties and [van der Meer et al. \(2014\)](#) therefore developed a different method: Because the amount of subduction (slab flux) must approximate seafloor production through time, they argued that *subduction lengths* could be used as a proxy for plate tectonic degassing. However, use of subduction lengths as a proxy for the slab flux (e.g. [Mills et al. 2017](#)) requires that the average rate of subduction remain constant through time, whereas most plate models suggest that high slab fluxes are linked to higher subduction rates rather than to higher global subduction lengths ([Domeier & Torsvik 2018](#); [Hounslow et al. 2018](#); [Torsvik et al. 2021](#); [Marcilly et al. 2021](#)). Subduction flux can be quantified from full-plate models, which include both the continental and oceanic components of plates and their boundaries ([Fig. 6b](#)), but before 200 Ma there is no *in-situ* oceanic lithosphere preserved and the remaining ~30% of the surface is continental lithosphere that only can be reconstructed with palaeomagnetic data. Longitude calibrations of paleomagnetic data to derive ‘absolute reconstructions’, however, differ widely before Pangea formed (320 Ma) and estimates of subduction flux from full-plate models must be considered with caution before the Devonian. Full-plate models have been developed back to 1 Ga ([Merdith et al. 2021](#)) and longer ([Li et al. 2023](#)), but they are largely ‘made up’ (synthetic) and estimates of pre-Phanerozoic subduction flux from these models are extremely different and can differ up to 300% during the Neoproterozoic.

To constrain  $f_{SR}$  more objectively in deep time, [Marcilly et al. \(2021\)](#) developed a continental arc-based zircon frequency curve that was scaled to normalized subduction flux for the past 350 Myrs ([Fig. 6b](#)). This is the hybrid  $f_{SR}$  used in Model 12 of [Marcilly et al. \(2021\)](#) and the arc-zircon based proxy for  $f_{SR}$  differ much from the estimated subduction flux from the [Merdith et al. \(2021\)](#) model in pre-Devonian times.  $f_{SR}$  for a specific model can be changed directly in the ‘*GEOCARB\_input\_arrays*’ file (located in the main GEOCARB\_NET folder), but in the ‘*Time-Series*’ menu one can also ‘*Change Entire Columns*’ and ‘*Replace fSR (plate tectonic degassing)*’ with precompiled  $f_{SR}$  estimates ([Fig. 3a](#)). These include two hybrid versions (combining subduction flux and scaled/normalized zircon frequency from arc-environments), a third curve is only based on arc-zircon frequency, and a fourth curve is based on subduction flux estimated from the [Merdith et al. \(2021\)](#) model. The data can also be found in the file ‘*Library\_fSR\_Plate\_Tectonic\_Degassing.csv*’ (located in /Geocarb\_Net/Library).

[Figure 6a](#) show differences in predicted  $p\text{CO}_2$  levels for the past 540 Myrs based on two different  $f_{SR}$  curves ([Fig. 6b](#)). One is the hybrid  $f_{SR}$  curve of [Marcilly et al. \(2021\)](#) and the second  $f_{SR}$  curve is the estimated subduction flux from the [Merdith et al. \(2021\)](#) full-plate model. The effect of using different proxies for  $f_{SR}$  to estimate  $p\text{CO}_2$  are in the order of thousands of ppm: The largest difference in predicted  $p\text{CO}_2$  is noted in the Cambrian at around 510 Ma (3216 ppm) but there are also pronounced differences during the Late Ordovician-Early Devonian and the early Mesozoic.

Variations in arc-related magmatism may have played a key role in regulating long-term climate change, and for example, [McKenzie et al. \(2016\)](#) claim that *all* icehouse climates can be explained by reduced arc activity (low CO<sub>2</sub> sourcing). The hybrid  $f_{SR}$  [Marcilly et al. \(2021\)](#) curve do show reduced subduction flux associated with icehouse climates (red arrows in [Fig. 6b](#)) but some of the lowest fluxes are noted during Early Mesozoic greenhouse climates (Triassic-Jurassic). Also note that the estimated  $f_{SR}$  from the [Merdith et al. \(2021\)](#) plate model yield very high values near the Ordovician-Silurian boundary ([Fig. 6b](#); the highest of the entire Palaeozoic), which results in much higher CO<sub>2</sub> levels (~2000 ppm) near the Hirnantian glaciation ([Fig. 6a](#)).

### 3.2 Changing CO<sub>2</sub> sinks

Silicate weathering activity is dictated by different ‘tectonic’ forcings such as the effect of relief on the weathering rate ( $f_R$ ), exposed land area ( $f_A$ ), the fraction of exposed land undergoing chemical weathering ( $f_{AW}/f_A$ ), and in part runoff ( $f_D$ ).

$f_A$  is expressed as the time-dependent total exposed land area relative to the presently exposed land area ( $149 \times 10^6 \text{ km}^2$ ):

$$f_A = \frac{\text{exposed land } t}{149 \times 10^6} \quad (\text{Equation 1})$$

We use estimates of exposed land (in 10 Myr interval) back to 520 Ma ([Marcilly et al. 2021](#)) and 540 Ma ([Marcilly 2022](#)), but refined estimates for  $f_A$  and other parameters are included in our ‘Latest Model (M12)’ and listed in the file ‘Library\_Weathering\_Arrays\_New’ (located in sub-folder /Library). Our refined maps of exposed land can be displayed in the ‘Map’ menu ([Fig. 3a](#)), and as an example, we show a palaeomagnetic based Pangea reconstruction at 230 Ma ([Fig. 7](#)) when global sea level was low, and consequently much exposed land at that time.

The  $f_{AW}/f_A$  parameter (fraction of exposed land undergoing chemical weathering relative today) was introduced by Royer *et al.* (2014) and based on GEOCLIM simulations to determine the fraction of land-area that had non-zero runoff. But the input for those simulations included only 22 Phanerozoic paleogeographic maps ([Goddéris et al. 2014](#)) and thus large extrapolations were required. As a supplement to computationally intensive 3D climate simulations, [Marcilly et al. \(2021\)](#) parameterized theoretical silicate weathering based on the latitudinal distribution of exposed land from paleogeographic maps in 10 Myrs intervals. For  $f_{AW}/f_A$ , [Marcilly et al. \(2021\)](#) estimated the amount of exposed land at latitudes with a high theoretical weatherability through time, and its expression can be written as:

$$f_{AW}/f_A = \frac{\left( \frac{\text{exposed land at high weathering latitudes } t}{\text{total exposed land } t} \right)}{\left( \frac{\text{exposed land at high weathering latitudes } t=0}{\text{total exposed land } t=0} \right)} \quad (\text{Equation 2})$$

215 Exposed rocks in warm and wet environments weather fastest, mostly within  $10^{\circ}$  of the equator, and  
 216 [Marcilly et al. \(2021\)](#) therefore considered exposed land with  $\pm 10^{\circ}$  as a reasonable proxy for ‘exposed  
 217 land at high weathering rates’ in Equation 2 but they also considered exposed land with  $\pm 10^{\circ}$  plus  
 218 exposed land between  $40$  and  $50^{\circ}\text{N/S}$  (their model M1, [Appendix 1](#)) as a proxy for  $f_{\text{AW}}/f_{\text{A}}$ . These  
 219 procedures assume constant climate belts through time, and they also introduced a third parametrization  
 220 procedure where they adjusted for arid equatorial regions developed during Pangea. This is witnessed  
 221 by the occurrences of extensive ‘tropical’ evaporites and lack of coal and bauxites in the central parts  
 222 of Pangea, e.g., during the Triassic ([Fig. 7](#)), which reduced the global weatherability ([Marcilly et al.](#)  
 223 [2021](#): Models 10-12). Applying an arid correction changes  $f_{\text{AW}}/f_{\text{A}}$  substantially ([Fig. 8c](#)) — *and results*  
 224 *in much higher CO<sub>2</sub> levels during the early Mesozoic (2733 ppm @ 250 Ma).*

225 In ‘Time Series’ and ‘Change Entire columns’, revised estimates of  $f_{\text{AW}}/f_{\text{A}}$  based on exposed land  
 226 within  $\pm 10^{\circ}$ , and with or without ‘arid correction’ ([Fig. 8b](#)), can be used to test or refine your carbon-  
 227 cycle model but we have also included estimates of  $f_{\text{AW}}/f_{\text{A}}$  where the amount of exposed land within  $\pm$   
 228  $10^{\circ}$  have been estimated from two different global reconstructions, namely [Scotese \(2019\)](#) and [Merdith](#)  
 229 [et al. \(2021\)](#). The amount of exposed land within  $\pm 10^{\circ}$  differ the most during the Paleozoic ([Fig. 8c](#))  
 230 and *with predicted CO<sub>2</sub> levels differing almost 6000 ppm during the Cambrian (Fig. 8a).*

#### 231 4. Land temperature and sensitivity testing of time-series

232 GEOG is the change in the mean land-surface temperature that is undergoing chemical weathering  
 233 relative to present day. GEOG is largely affected by changes in paleogeography, originally formulated  
 234 from global circulation modelling (GCM) in [Otto-Bliesner \(1995\)](#) but revised in [Royer et al. \(2014\)](#)  
 235 based on GCM simulations in [Godderis et al. \(2012\)](#). The revised Phanerozoic GEOG curve is  
 236 essentially warmer during the Mesozoic and cooler during the early-mid Paleozoic ([Fig. 9b](#)). In ‘Time  
 237 Series’ and ‘Change Entire columns’, you can ‘Replace GEOG\_G (Godderis) with GEOG Berner’ and  
 238 the difference in predicted CO<sub>2</sub> levels for these two temperature curves is shown in [Figure 9a](#). The  
 239 cooler early Paleozoic land temperatures strongly reduce silicate weathering efficiency and elevate CO<sub>2</sub>  
 240 predictions by almost 5000 ppm at 540 Ma. Differences are small between 430 to 260 Ma but for the  
 241 Mesozoic there are significant episodes of both higher (250 Ma) or lower (130 Ma) predicted CO<sub>2</sub> levels  
 242 when using the revised GEOG (‘Godderis’) curve.

243 In GEOCARB\_NET we have also implemented a routine to “Set one or several time-series values  
 244 to present-day” ([Fig. 9c](#)) to test their influence on predicted CO<sub>2</sub> calculations. This option is selected  
 245 through ‘Time Series’ and ‘Change Entire columns’ and as an example we show the effect of assuming  
 246 that GEOG did not change relative to today (GEOG is zero all times). Compared with our default GEOG  
 247 (‘Godderis’) formulation (curve 1 in [Fig. 9a](#)) there are only minor differences between 500 and 210 Ma  
 248 but pronounced difference are noted for the early Cambrian and large parts of the Mesozoic (notably at  
 249 130 Ma). GEOCARB\_NET is not much sensitive to parameter changes for the past 100 Myrs but

250 assuming a somewhat cooler Late Cretaceous Earth will effectively elevate predicted CO<sub>2</sub> levels.  
 251 Conversely, a slightly warmer Ordovician world can reduce CO<sub>2</sub> levels across the Hirnantian glaciation.

## 252 **5. Land-assisted weathering parameters**

253 Land plants arose during the Ordovician, but vascular plants first started to colonize the land in the  
 254 early Silurian, and through the latest Silurian-Devonian they became a major factor in powering the  
 255 substantial changes within the terrestrial environments (Pawlick *et al.* 2020; Wellman *et al.* 2022; Capel  
 256 *et al.* 2023). A particularly striking change was the progressive increase in height, from relatively small  
 257 leafless plants up to large trees and forests (Stein *et al.* 2020), and by the end of the Devonian, forests  
 258 were as widespread as they are today.

259 Large vascular plants with extensive root systems weather rocks faster than the algae or lichens that  
 260 preceded them (Berner 1998, 2004, Berner & Kothavala 2001), and the weathering forcing in  
 261 GEOCARB\_NET is strongly sensitive to the land-assisted weathering parameter LIFE (rate of chemical  
 262 weathering in a minimally vegetated world relative to present-day). This can be tested as follows: First  
 263 ‘Run Model’ with ‘error analysis’ (example in Fig. 10a uses Marcilly *et al.* 2021, model 12), then engage  
 264 ‘Edit’ and ‘Constants’ and change ‘LIFE’ to 0.125 (lower bound of the 2σ error, equivalent to an eight-  
 265 fold increase in chemical weathering due to large land plants). In ‘Organize’ select ‘Save changes (and  
 266 exit)’ and then ‘Run Model’. This will elevate all the predicted CO<sub>2</sub> levels before 350 Ma. By repeating  
 267 this procedure but assigning ‘LIFE’ a value of 0.375 (higher bound, equivalent to a 2.7-fold  
 268 amplification), one can reproduce parts of Fig. 10a where the predicted CO<sub>2</sub> levels of varying the LIFE  
 269 parameter lies within the green shaded region, affecting CO<sub>2</sub> levels from 360 Ma and backwards, and  
 270 with huge differences of about 12000 ppm at the dawn of the Phanerozoic (540 Ma).

271 Another important land-assisted weathering parameter is GYM, the rate of chemical weathering by  
 272 gymnosperms relative to the angiosperms (flowering plants), the latter which dominate the present-day  
 273 world. In ‘Organize’, select ‘Restore System’ and ‘Marcilly *et al.* (2021: M12)’, engage Edit’ and  
 274 ‘Constants’ and the change ‘GYM’ to its lower bound value (0.459). ‘Save changes (and exit)’, then  
 275 ‘RUN MODEL’ and notice elevated CO<sub>2</sub> predictions between 370 and 90 Ma. Repeat this procedure,  
 276 assign ‘GYM’ a value of 1.290 (highest value within error bounds) and we can the reproduce parts of  
 277 Fig. 10a where the predicted CO<sub>2</sub> levels of varying GYM lies within the yellow shaded region (90-370  
 278 Ma). A massive difference — about 12000 ppm — is noted at 250 Ma.

279 In Figure 10a we also show the variation in predicted CO<sub>2</sub> levels by varying the land-assisted  
 280 weathering parameter FERT (exponent reflecting the fraction of vegetation whose growth is stimulated  
 281 by elevated CO<sub>2</sub>). Changes in FERT (between 100 and 380 Ma) is less sensitive than LIFE and GYM  
 282 but yield differences in predicted CO<sub>2</sub> as high as 2000 ppm (250 Ma) and 1400 ppm (130 Ma).

## 283 **6. Modifying climate sensitivity**

284 Climate sensitivity (i.e., temperature change per doubling of CO<sub>2</sub>) is an import parameter in carbon-  
 285 cycle modelling and GCMs. On geological time scales it is not constant, but in many models, it is set  
 286 to a fixed value of 4.5° (e.g., COPSE). In GEOCARB\_NET, as in previous GEOCARB version, climate  
 287 sensitivity (constant named deltaT2X; Fig. 11) defaults to 3° for greenhouse climates, and a constant  
 288 named GLAC is a factor by which deltaT2X changes during icehouse climates. GLAC defaults to 2,  
 289 and thus greenhouse and icehouse climates are modelled with a climate sensitivity of 3 and 6°,  
 290 respectively (Park & Royer 2011; Wong *et al.* 2021). The GLAC and deltaT2X constants are stored in  
 291 'GEOCARB\_input\_summaries.csv' but can be changed through options 'Edit' and 'Constants' (Figs.  
 292 3a, 11). After making changes select 'Save Changes (and Exit)' in the constant 'Organize' menu and  
 293 then 'Run Model' to test the effect of changes in deltaT2X and GLAC (Fig. 11). Periods of icehouse  
 294 climates defaults to 330-260 Ma (LPIA) and 34-0 Ma (ECIA) as in earlier GEOCARB versions but we  
 295 have introduced a new option to simulate icehouse climates during the short-lived Hirnantian glaciation  
 296 by also changing deltaT2X (according to GLAC) in late Ordovician-Early Silurian times (450-440 Ma).

297 In all the previous examples we ran the Marcilly *et al.* (2012: M12) model with icehouse climates  
 298 imposed between 330-260 and 40-0 Ma (deltaT2X=6), but by imposing a higher climate sensitivity  
 299 between 450 and 440 Ma, the predicted CO<sub>2</sub> levels across the Hirnantian is much reduced and falls  
 300 below the theoretical threshold for glacial inception. We also show examples of running the Marcilly  
 301 *et al.* (2012, M12) with constant climate sensitivity: Using a constant sensitivity of 6° leads to low CO<sub>2</sub>  
 302 predictions for most of the Phanerozoic (brown curve in Fig. 11) and predicted CO<sub>2</sub> differences (6°  
 303 versus 3°) are as high as 6643 ppm at 540 Ma.

## 304 7. CO<sub>2</sub> and temperature proxies

305 Atmospheric CO<sub>2</sub> concentrations can be estimated from proxies, e.g., δ<sup>13</sup>C of paleosols, marine  
 306 phytoplankton, long chained alkenones in haptophytic algae, liverworts, stomatal densities and indices  
 307 in plants, and δ<sup>11</sup>B of marine carbonate (Royer 2006, The CenCO2PIP Consortium 2023). We have  
 308 averaged these proxy systems based on the most reliable Cenozoic proxies (The CenCO2PIP  
 309 Consortium, 2023), which has been combined back in time with the most up-to date Paleozoic-  
 310 Mesozoic compilation of Dana Royer [a refinement of the Foster *et al.* (2017) data compilation] and  
 311 phytoplankton proxies (Witkowski *et al.* 2018). In total, our new binned CO<sub>2</sub> proxy curve back to 450  
 312 Ma (Fig. 12a, b) is based on more than 2500 proxies from phytoplankton (N=832), boron (805),  
 313 paleosols (555), stomata (286) and a subordinate number of alkenones (23) and liverworts (15). The  
 314 proxy file is named "Royer2018\_VC\_PP\_Raw\_CO2.csv" (located in subfolder /proxies) and a global  
 315 running mean curve (10 Myr bins) is dubbed "Royer2018\_VC\_PP\_Binned10\_CO2.csv". The latter file  
 316 contains mean values, 1σ standard deviation (SD) and the number of proxies for each mean value. The  
 317 binned curve is by default shown with 95% confidence errors based on standard errors (SE = SD/√N)  
 318 but can be displayed with SD 95% confidence errors, which is selected in the 'Proxies' panel (Figs. 3b,

319 4). We have also included the LOESS fitted curve of [Foster et al. \(2017\)](#), which is broadly like the  
 320 binned proxy curve between 420 and 100 Ma.

321 CO<sub>2</sub> proxies are most reliable since the Early Devonian (~420 Ma) since the average proxy curve  
 322 before that time is based on a single proxy (phytoplankton; [Wikowski et al. 2019](#)). The binned proxy  
 323 curve ([Fig. 12b](#)) shows peak atmospheric CO<sub>2</sub> concentrations of about 2000 ppm during the Devonian  
 324 and the Triassic, a peak value of 1600 ppm is recognized in the early Eocene, and collectively the mean  
 325 Phanerozoic greenhouse CO<sub>2</sub> level is 1100 ppm. The three icehouses are characterized by low CO<sub>2</sub>,  
 326 about 600 ppm across the Hirnantian (450-440 Ma) whilst the LPIA and ECIA average ~450 and 350  
 327 ppm, respectively. Near the Pliocene-Pleistocene boundary (2.6 Ma) when our planet approached the  
 328 current icehouse with bipolar glaciation, CO<sub>2</sub> levels dropped below 270 ppm ([Fig. 12a](#); [The CenCO2PIP  
 329 Consortium, 2023](#)). Compared with our refined model 12 of [Marcilly et al. \(2021\)](#) with modified climate  
 330 sensitivity across the Hirnantian ([Section 6](#)), the modelled and CO<sub>2</sub> proxy curves are broadly similar  
 331 but there is clear difference in the early Mesozoic (early Triassic) and late Cretaceous-Early Neogene  
 332 times.

333 Since CO<sub>2</sub> is considered a key greenhouse gas in modulating atmospheric temperature, we have  
 334 implemented temperature data sets in GEOCARB\_NET for comparing CO<sub>2</sub> and temperature trends,  
 335 which can also be used to explore climate sensitivity. One data set includes sea surface temperatures  
 336 (SSTs, [Fig. 12c](#)) based on δ<sup>18</sup>O measurement from phosphate fossils until 245 Ma and from a blend of  
 337 phosphate and carbonate fossils after that time. We vetted the SST dataset of [Song et al. \(2019\)](#) and  
 338 extended it from 498 Ma to 520 Ma with δ<sup>18</sup>O data from phosphatic Siberian brachiopods ([Wotte et al.  
 339 2019](#)). Only fossils that once lived within 30° of the equator were included and some anomalous SSTs  
 340 have been excluded ([Zhang & Torsvik 2022](#); [Scotese et al. 2021](#)). A second data set includes global  
 341 average temperatures (GATs; [Scotese et al. 2021](#)), which is based on an area-scaled integration of all  
 342 the climate belts derived from plate reconstructions (biome maps) combined with SST constraints and  
 343 some ad hoc corrections. Both datasets are found in “*SST\_5Ma\_Binns\_Latitude\_0\_30\_and  
 344 GAT\_Scotese2021\_5Ma\_Intervals.csv*”, which is in the */Temperature* folder ([Fig. 2a](#)). The SST curve  
 345 is a running mean curve (5 Myr bins) and listed in 5 Myr intervals. The mean GAT curve is also listed  
 346 in 5 Myrs intervals: it is broadly like the SSTs for the past 350 Myrs, but in the early Paleozoic, the  
 347 GAT temperatures are much lower ([Fig. 3b, 12b](#)).

348 Across time scales of tens of millions of years, the pattern of reconstructed CO<sub>2</sub> levels is broadly  
 349 coherent with SSTs trends, e.g., from the late Devonian to the mid-Permian (370-270 Ma), from the  
 350 mid-Triassic to the early Cretaceous (230-120 Ma), and for the past 80 Myrs. This suggests a link  
 351 between CO<sub>2</sub> and temperature but there are clear exceptions during the Devonian and the late Permian-  
 352 Early Triassic. The very low average SSTs seen for the LPIA and the ECIA is not clearly recognized  
 353 during the Hirnantian. The Hirnantian, however, was very short-lived, our mean SST curve is also  
 354 smoothed (5 Myr bins), but there are a few SSTs from South China that show very low ‘icehouse-like’  
 355 temperatures (7-12°) between 445 and 444.4 Ma. Conversely, the GAT curve shows a pronounce dip

356 during the Hirnantian, but this is an ad hoc GAT correction as stated in [Scotese et al. \(2021\)](#): “we have  
 357 exaggerated the dip in temperature to help explain the growth of the massive, Hirnantian south polar  
 358 ice cap”.

359 A pronounced CO<sub>2</sub> proxy peak in the early Devonian ([Fig. 12b](#)) is not recognized in SSTs or GATs  
 360 ([Fig. 12c](#)) but unfortunately there is a large data gap in the SSTs (420-400 Ma) when restricted by δ<sup>18</sup>O  
 361 data from reconstructed fossils within 30° of the equator. There is also an apparent mismatch in the late  
 362 Permian-early Triassic when CO<sub>2</sub> proxy values are low, and temperatures are high. Conversely,  
 363 modelled CO<sub>2</sub> values are much higher than the proxy values. In more recent times, the mid-Oligocene-  
 364 early Miocene is also enigmatic ([Fig. 12a](#)) as there are relatively large variations in the CO<sub>2</sub> proxies  
 365 with very minor temperature changes, which implies near-zero climate sensitivity ([The CenCO2PIP  
 Consortium 2023](#)).

## 367 8. Discussion and future outlooks

368 GEOCARB\_NET is a user-friendly carbon-cycle modelling tool but also contains extensive libraries  
 369 of models and proxy data. We have described how to use GEOCARB\_NET in the context of  
 370 Phanerozoic climate change and specifically addressed how some key input parameters affect  
 371 reconstructed CO<sub>2</sub> levels for the past 540 Myrs. GEOCARB\_NET can be run back to 570 Ma but the  
 372 parametrization of many time-series is uncertain before 540 Ma. This includes the amount and spatial  
 373 distribution of exposed land (strongly controlling runoff and silicate weathering) and the fact that global  
 374 plate reconstructions are very unreliable during the Ediacaran ([Domeier et al. 2022](#)). We therefore need  
 375 better plate models with maps of exposed lands to extend GEOCARB\_NET (and other carbon-cycle  
 376 models) into the deep past.

377 Assigning reliable error envelopes to CO<sub>2</sub> estimates is not trivial and we opted for a simple  
 378 percentage error routine. Assigning a 4% error on key individual parameters reproduce the ‘inner bands’  
 379 in the Monte Carlo simulations of [Royer et al. \(2014\)](#). Values of 6-8% mimics most of the spread or  
 380 variance ([Fig. 13b](#)) in our examples, which is largely controlled by six parameters, the plant-assisted  
 381 weathering factors LIFE (Palaeozoic) and GYM (Mesozoic), climate sensitivity, fraction of exposed  
 382 land undergoing chemical weathering ( $f_{AW}/f_A$ ), change in the mean land-surface temperature undergoing  
 383 chemical weathering (GEOG) and ‘plate tectonic’ degassing ( $f_{SR}$ ). CO<sub>2</sub> spread can at times be very  
 384 large, notably during the Cambrian (~15000 ppm), the Devonian (~7000 ppm), the early Triassic  
 385 (~12000 ppm) and the early Cretaceous (~9000 ppm) greenhouses.

386 The median CO<sub>2</sub> curve is based on model 12 of [Marcilly et al. \(2021\)](#), which we have updated with  
 387 refined estimates of silicate weathering ( $f_A, f_{AW}/f_A$ ) as well as extended the model from 520 to 540 Ma.  
 388 We have also implemented an ‘Hirnantian’ option to model the end-Ordovician glaciation with a  
 389 different climate sensitivity as the other Phanerozoic icehouses (defaults to 6° per doubling of CO<sub>2</sub>).  
 390 This leads to modelled Hirnantian CO<sub>2</sub> levels that are compatible with CO<sub>2</sub> proxies (phytoplankton)  
 391 and well below estimated thresholds for glacial inception (~1000 ppm) at that time. This is also the case

for the LPIA and the ECIA, but GEOCARB\_NET (as all previous GEOCARB models) yields low ‘icehouse-like’ CO<sub>2</sub> levels for the past 110 Myrs and which are systematically lower than CO<sub>2</sub> proxy values (Fig. 13b). In our examples, only a reduction in GEOG can raise CO<sub>2</sub> model predictions in the Late Cretaceous-Early Cenozoic. In GEOCARB\_NET one can easily change the parametrization to increase/decrease modelled CO<sub>2</sub> values. As an example, one could experiment with the effect of carbonate content of subducting oceanic crust on CO<sub>2</sub> degassing relative today. This time-dependent parameter is named  $f_C$  and simply assigned a constant value of 0.75 before 150 Ma and ramped up linearly to 1 for present day (Berner 2004). Conversely, if we assume that this effect was much higher in the Cretaceous and Paleogene (100-30 Ma) we can match the model-proxy record by increasing  $f_C$  to about 3 times its present value, *but is this realistic?* There are also other model-proxy mismatches, including the early Triassic and early Cretaceous, but in both cases, increasing the weathering efficiency (e.g.) can rectify models and proxies.

GEOCARB\_NET also estimates atmospheric O<sub>2</sub>, but we here focus on CO<sub>2</sub> since oxygen predictions are largely influenced by isotopic proxy data and not ‘tectonic’ parametrizations. There are three input time-series (Sr, δ<sup>13</sup>C, δ<sup>34</sup>S; Fig. 2b) dealing with isotopic proxy data, but reconstructed O<sub>2</sub> levels (Fig. 13a) largely mirror changes in the stable carbon (δ<sup>13</sup>C) isotopic composition of shallow-marine carbonates (δ<sup>13</sup>C<sub>Carb</sub>; Appendix 1). Updating the default GEOCARB\_NET δ<sup>13</sup>C<sub>Carb</sub> record of Berner (2004, 2006a, 2009) with that of Carmer & Jarvis (2020) leads to model failures (see Mills et al. (2022)) unless the δ<sup>13</sup>C<sub>Carb</sub> record is much smoothed. Using a Savitzky-Golay filtered record to avoid model failure over most of the Phanerozoic we notice a dramatic difference in O<sub>2</sub> levels during the Permo-Carboniferous (almost 20% drop in predicted oxygen levels at 290 Ma), which needs to be explored and understood in future studies. Conversely, updating the δ<sup>13</sup>C<sub>Carb</sub> record in GEOCARB\_NET has very little effects on reconstructed CO<sub>2</sub> levels, except for the early Triassic (Fig. 13a).

GEOCARB\_NET and other carbon-cycle models such as COPSE, GEOCLIM and SCION (e.g., Lenton et al. 2018; Godderis et al. 2014; Mills et al. 2021) predict large differences in both CO<sub>2</sub> and O<sub>2</sub>. Reconstructed CO<sub>2</sub> levels in these models undoubtedly reflect the parametrization of plate tectonic degassing, silicate weathering and climate sensitivity. As an example, we ran a COPSE model (Lenton et al. 2019) with parametrizations as in Marcilly et al. (2021, Model 12), i.e., similar  $f_{SR}$  (named XX in COPSE) and **weathering // Chloe explains** and we used climate sensitivities of 3 and 6° for greenhouse and icehouses, respectively. We also adapted a 6° climate sensitivity across the Hirnantian. The original COPSE (ran with a constant climate sensitivity of 4.5°) and a hybrid model (COPSE-H) ran with different parametrizations can be selected in the ‘Models’ panel. The COPSE model of Lenton et al. (2019) predicts peak CO<sub>2</sub> values of 3300 ppm in the early Paleozoic (480 Ma) and, overall, predicted CO<sub>2</sub> levels are about half of those predicted by GEOCARB\_NET over the past 520 Myrs (Fig. 13c). After implementing the parametrization changes described above, the two models become much more similar, a Pearson r-correlation of 0.87 demonstrates a strong positive relationship between the two model results, but a detailed benchmarking of carbon-cycle models is urgently required.

429 Carbon-cycle models are essential to reconstruct changes in atmospheric CO<sub>2</sub> concentrations and  
 430 GEOCARB\_NET should prove useful for both academic research and educational purposes. The  
 431 current version is a desktop version, but plans include development of an interactive web-based version.  
 432 We also plan to implement the SCION model ([Mills et al. 2021](#)) in GEOCARB\_NET, and thus in the  
 433 future we envision that several carbon-cycle models can be tested and compared within the same GUI  
 434 package.

435

#### 436 Acknowledgements

437 The Research Council of Norway (RCN), through its Centers of Excellence funding scheme, project  
 438 number 332523 (PHAB) is acknowledged for financial support.

439

#### 440 References

- 441 Berner, R.A., Lasaga, A.C., & Garrels, R.M. (1983). The carbonate silicate geochemical cycle and its  
 442 effect on atmospheric carbon dioxide over the past 100 million years. *American Journal Science*,  
 443 283, 641–683
- 444 Berner, R.A., 1991. A model for atmospheric CO<sub>2</sub> over Phanerozoic time. *American Journal of Science*  
 445 291, 339-376. doi: 10.2475/ajs.291.4.339
- 446 Berner R.A., 1998. The carbon cycle and CO<sub>2</sub> over Phanerozoic time: the role of land plants. *Phil.  
 447 Trans. R. Soc. Lond. B* 353:75–82.
- 448 Berner, R. A. & Kothavala, Z. 2001 GEOCARB III; a revised model of atmospheric CO<sub>2</sub> over  
 449 Phanerozoic time. *Am. J. Sci.* 301, 182–204. (doi:[10.2475/ajs.301.2.182](https://doi.org/10.2475/ajs.301.2.182))
- 450 Berner, R.A., 2004. The Phanerozoic Carbon Cycle: CO<sub>2</sub> and O<sub>2</sub>: New York, Oxford University Press,  
 451 150 p.
- 452 Berner, R.A., 2006a. Inclusion of the weathering of volcanic rocks in the GEOCARBSULF model.  
 453 *American Journal of Science* 306, 295-302. doi: 10.2475/05.2006.01
- 454 Berner, R.A., 2006b. GEOCARBSULF: A combined model for Phanerozoic atmospheric O<sub>2</sub> and CO<sub>2</sub>.  
 455 *Geochimica et Cosmochimica Acta* 70, 5653-5664. doi: 10.1016/j.gca.2005.11.032.
- 456 Bierman, P.R., Corbett, L.B., Graly, J.A. et al. 2014. Preservation of a Preglacial Landscape Under the  
 457 Center of the Greenland Ice Sheet. *Science* 344, 402–405.
- 458 Capel, E., Cleal, C. J., Servais, T., & Cascales-Miñana, B. (2023). New insights into Silurian–Devonian  
 459 palaeophytogeography. *Palaeogeography, Palaeoclimatology, Palaeoecology*, 613, 111393
- 460 Catling & Zahnle 2020. The Archean atmosphere. *Sci. Adv.* 6: eaax1420.
- 461 DeConto, R. M. & Pollard, D. 2003. Rapid Cenozoic glaciation of Antarctica induced by declining  
 462 atmospheric CO<sub>2</sub>. *Nature* 421, 245–249.
- 463 De Schepper, S., Gibbard, P.L., Salzmann, U. & Ehlers, J. 2014. A global synthesis of the marine and  
 464 terrestrial evidence for glaciation during the Pliocene Epoch. *Earth-Sci. Rev.* 135, 83–102.

- 465 Domeier, M. & Torsvik, T.H. 2017. Full-plate modelling in pre-Jurassic time. *Geol. Mag.*  
 466 doi:10.1017/S0016756817001005.
- 467 Domeier, M., Magni, V., Hounslow, M.W., Torsvik, T.H., 2018. Episodic zircon age spectra mimic  
 468 fluctuations in subduction. *Sci. Rep.* 8, 1747. <https://doi.org/10.1038/s41598-018-35040-z>.
- 469 Foster, G.L., Royer, D.L., Lunt, D.J., 2017. Future climate forcing potentially without precedent in the  
 470 last 420 million years. *Nature Commun.* 8, 14845.
- 471 Gibbs, M.T., Bice, K.L., Barron, E.J., & Kump, L.R. (2000). Glaciation in the early Paleozoic  
 472 ‘greenhouse’: the roles of paleogeography and atmospheric CO<sub>2</sub>. In Huber, B.T., MacLeod, K. G.,  
 473 & Wing, S.L. (Eds.), *Warm Climates in Earth History* (pp. 386–422). Cambridge, Cambridge  
 474 University Press.
- 475 Goddériss, Y., Donnadieu, Y., Le Hir, G., Lefebvre, V., Nardin, E., 2014. The role of paleogeography  
 476 in the Phanerozoic history of atmospheric CO<sub>2</sub> and climate. *Earth Sci. Rev.* 128, 122–138.  
 477 <https://doi.org/10.1016/j.earscirev.2013.11.004>.
- 478 Goddériss, Y., Donnadieu, Y. 2019. A sink- or a source-driven carbon cycle at the geological timescale?  
 479 Relative importance of palaeogeography versus solid Earth degassing rate in the Phanerozoic  
 480 climatic evolution. *Geol. Mag.* 156 (2), 355–365.
- 481 Hoffman *et al.* 2018. Snowball Earth climate dynamics. *Sci. Adv.* 3, e1600983.
- 482 Hounslow, M., Domeier, M. & Biggin, A.J. 2018. Subduction flux modulates the geomagnetic polarity  
 483 reversal rate. *Tectonophysics* 742-743, 34-49
- 484 Lenton, T.M., Daines, S.J., Mills, B.J.W. 2018. COPSE reloaded on an improved model of  
 485 biogeochemical cycling over Phanerozoic time. *Earth Sci. Rev.* 178, 1-28.
- 486 Li, Z-X, Liu, Y. & Richard Ernst, 2023. A dynamic 2000—540 Ma Earth history: From cratonic  
 487 amalgamation to the age of supercontinent cycle. *Earth-Science Reviews* 238, 104336.
- 488 Marcilly, C.M., Torsvik, T.H., Domeier, M., Royer, D.L., 2021. New paleogeographic and degassing  
 489 parameters for long-term carbon cycle models. *Gondwana Research* 97, 176–203.  
 490 <https://doi.org/10.1016/j.gr.2021.05.016>.
- 491 Marshall, H.G., Walker, J.C.G., & Kuhn, W.R. (1988). Longterm climate change and the geochemical  
 492 cycle of carbon. *Journal of Geophysical Research*, 93, 791–801.
- 493 McKenzie, N.R., Horton, B.K., Loomis, S.E. et al. 2016. Continental arc volcanism as the principal  
 494 driver of icehouse-greenhouse variability. *Science* 352, 444-447.
- 495 Merdith, A.S., Williams, S.E., Collins, A.S., Tetley, M.G., Mulder, J.A., Blades, M.L., Young, A.,  
 496 Armistead, S.E., Cannon, J., Zahirovic, S., Müller, R.D., 2021. Extending full-plate tectonic models  
 497 into deep time: Linking the Neoproterozoic and the Phanerozoic. *Earth Sci. Rev.* 214.  
 498 <https://doi.org/10.1016/j.earscirev.2020.103477>.
- 499 Mills, B.J.W. Scotese, C.R., Walding, N.G., Shields, G.A. & Lenton, T.M. 2017. Elevated CO<sub>2</sub>  
 500 degassing rates prevented the return of Snowball Earth during the Phanerozoic. *Nature Comm.* DOI:  
 501 10.1038/s41467-017-01456-w

- 502 Mills, B.J.W., Donnadieu, Y., Goddérés, Y. 2021. Spatial continuous integration of Phanerozoic global  
 503 biogeochemistry and climate. *Gondwana Research* 100, 73-86.
- 504 Otto-Bliesner, B. L., 1995, Continental drift, runoff and weathering feedbacks: Implications from  
 505 climate model experiments: *Journal of Geophysical Research*, v. 100, n. D6, p. 11537–11548,  
 506 <http://dx.doi.org/10.1029/95JD00591>
- 507 Park, J., and Royer, D. L., 2011, Geologic constraints on the glacial amplification of Phanerozoic  
 508 climate sensitivity: *American Journal of Science*, v. 311, p. 1-26, doi: 10.2475/01.2011.01.
- 509 Pawlik, Ł., Buma, B., Šamonil, P., Kvaček, J., Gałazka, A., Kohout, P., & Malik, I. (2020). Impact of  
 510 trees and forests on the Devonian landscape and weathering processes with implications to the global  
 511 Earth's system properties-A critical review. *Earth-Science Reviews*, 205, 103200.
- 512 Raymo, M.E., Ruddiman, W.F., & Froelich, P.N. 1988. Influence of late Cenozoic mountain building  
 513 on ocean geochemical cycles. *Geology*, 16, 649–653.
- 514 Royer, D.L., 2006. CO<sub>2</sub>-forced climate thresholds during the Phanerozoic. *Geochim. Cosmochim. Acta*  
 515 70 (23), 5665–5675. <https://doi.org/10.1016/j.gca.2005.11.031>.
- 516 Royer, D.L., Donnadieu, Y., Park, J., Kowalczyk, J., Goddérés, Y., 2014. Error analysis of CO<sub>2</sub> and O<sub>2</sub>  
 517 estimates from the long-term geochemical model GEOCARBSULF. *Am. J. Sci.* 314 (9), 1259–1283.
- 518 Royer, D.L., 2016. Climate sensitivity in the geologic past. *Annu. Rev. Earth Planet Sci.*, 44
- 519 Ruggieri, E., Herbert, T., Lawrence, K.T. & Lawrence, C.E. 2009. Change point method for detecting  
 520 regime shifts in paleoclimatic time series: application to δ<sup>18</sup>O time series of the Plio-Pleistocene.  
 521 *Paleoceanography* 24, <https://doi.org/10.1029/2007PA001568>.
- 522 Scotese, C.R. 2019.
- 523 Scotese, C.R., Song, H., Mills, B.J.W., van der Meer, D.G., 2021. Phanerozoic paleotemperatures: The  
 524 Earth's changing climate during the last 540 million years. *Earth Sci. Rev.*
- 525 Song, H., Wignall, P.B., Song, H., Dai, X., Chu, D., 2019. Seawater temperature and dissolved oxygen  
 526 over the past 500 million years. *J. Earth Sci.* 30 (2), 236–243.
- 527 Stein, W. E., Berry, C. M., Morris, J. L., Hernick, L. V., Mannolini, F., Ver Straeten, C., ... & Leake, J.  
 528 R. (2020). Mid-Devonian Archaeopteris roots signal revolutionary change in earliest fossil  
 529 forests. *Current biology*, 30(3), 421-431.
- 530 Stern 2018. The evolution of plate tectonics. *Phil. Trans. R. Soc.* 376, 20170406.
- 531 The CenCO2PIP Consortium, 2023. Toward a Cenozoic history of atmospheric CO<sub>2</sub>. *Science* 382,  
 532 1136.
- 533 Torsvik, T.H., Cocks, L.R.M., 2017. Earth History and Palaeogeography. Cambridge University Press,  
 534 p. 317 pp.
- 535 Torsvik, T. H., Svensen, H. H., Steinberger, B., Royer, D. L., Jerram, D. A., Jones, M. T., & Domeier,  
 536 M. 2021. Connecting the deep Earth and the atmosphere. In Mantle Convection and Surface  
 537 Expressions (Edited by Hauke Marquardt, Maxim Ballmer, Sanne Cottaar and Jasper Konter).

- 538      Geophysical Monograph 263, 413-453. American Geophysical Union. DOI:  
 539      10.1002/9781119528609.ch16.
- 540      Torsvik, T.H., Cocks, L.R.M, Dowding, E.M., Marcilly, C.M. & Domeier, 2023. Aspects of Devonian  
 541      Global Geography and Environments. ZDGG-Journal of Applied and Regional Geology, Special  
 542      Issue commemorating Leopold von Buch (invited paper).
- 543      Van der Meer, D.G, Zeebe, R., van Hinsbergen, D.J.J., Sluijs, A., Spakman, W., Torsvik, T.H., 2014.  
 544      Plate tectonic controls on atmospheric CO<sub>2</sub> levels since the Triassic. Proc. Natl. Acad. Sci.  
 545      doi:10.1073/pnas.1315657111.
- 546      Walker, J.C.G., Hays, P.B., & Kasting, J.F. (1981). A negative feedback mechanism for the long-term  
 547      stabilization of Earth's surface temperature. *Journal of Geophysical Research*, 86, 9776–9782.
- 548      Wellman, C. H., Berry, C. M., Davies, N. S., Lindemann, F. J., Marshall, J. E., & Wyatt, A. (2022).  
 549      Low tropical diversity during the adaptive radiation of early land plants. *Nature Plants* 8(2), 104-  
 550      109.
- 551      Witkowski, C.R., Weijers, J.W.H., Blais, B, Schouten, S., Sinninghe Damsté, J.S. 2018. Molecular  
 552      fossils from phytoplankton reveal secular PCO<sub>2</sub> trend over the Phanerozoic. *Sci. Adv.* 2018;4:  
 553      eaat4556.
- 554      Wong, T. E., Cui, Y., Royer, D. L., and Keller, K., 2021, A tighter constraint on Earth-system sensitivity  
 555      from long-term temperature and carbon-cycle observations: *Nature Communications*, v. 12, p. 3173,  
 556      doi: 10.1038/s41467-021-23543-9.
- 557      Wotte T., Skovsted C.B., Whitehouse M.J., Kouchinsky A., 2019. Isotopic evidence for temperate  
 558      oceans during the Cambrian Explosion. *Sci Rep.* 9(1):6330. doi: 10.1038/s41598-019-42719-4.
- 559      Zhang, H.R. & Torsvik, T.H. 2022. Circum-Tethyan magmatic provinces, shifting continents and  
 560      Permian climate change. *Earth Planet. Sci. Lett.* 584, 117453.
- 561

562 **FIGURE CAPTIONS**

563 **Figure 1.** Phanerozoic time scale, greenhouse vs. icehouse conditions and three models for atmospheric  
 564 CO<sub>2</sub> predicted from GEOCARBSULFvolc (Royer *et al.* 2014), COPSE (Lenton *et al.* 2019) and SCION  
 565 (Mills *et al.* 2022). The GEOCARBSULFvolc curve is shown with inner band confidence envelopes  
 566 (yellow shading). Models are compared with a running mean CO<sub>2</sub> proxy curve (10 Myr bins) for the  
 567 past 450 Myrs with 95% confidence error bars if N>1(Section 6) and with Cenozoic input data detailed  
 568 in The CenCO2PIP Consortium (2023). The blue stippled line is a theoretical CO<sub>2</sub> threshold to initiate  
 569 continental scale glaciations (see text). H, Hirnantian glacial event; LPIA, Late Paleozoic Ice Age (330-  
 570 260 Ma); ECIA, End Cenozoic Ice Age (34-0 Ma).

571 **FIGURE 2. (a)** Main programs, input & output files, and subfolders in *GEOCARB\_NET*. The main  
 572 GUI (*GEOCARB\_NET2023.EXE*) prepares the input files, runs the carbon-cycle modelling code  
 573 *GEOCARB\_LastRun.R* and display the output file ('*GEOCARB\_output.CVS*') generated by R-code. **(b)**  
 574 The input file '*GEOCARB\_Input\_arrays.CSV*' contain 12 different time-series and associated errors  
 575 (not shown in diagram) in 10 Myrs interval from 570 Ma to present. Four of these,  $f_A$ ,  $f_{AW}/f_A$ ,  $f_D$  and  
 576 GEOG were modified in Royer *et al.* (2014), and the input file contain both the values used before 2014  
 577 (Berner 2006a, b) and the new values named  $f_A$ \_Godderis etc (in diagram and software just  $f_A$ \_G for  
 578 simplicity). **(c)** There are two different formats for the '*GEOCARB\_Output*' file: If  
 579 '*GEOCARB\_NET2023*' is run without '*Error Analysis*', then there are three columns for each time step  
 580 [failed (run (%)), estimated CO<sub>2</sub> (ppm) and O<sub>2</sub> (%)]. Conversely, if a model is run with '*Error Analysis*'  
 581 then 5 columns are listed at each time-step [estimated CO<sub>2</sub> (ppm), LOW-CO<sub>2</sub> (ppm), HIGH-CO<sub>2</sub> (ppm),  
 582 cumulative ERROR (%) in CO<sub>2</sub> and O<sub>2</sub> (%)].

583 **FIGURE 3. (a)** Start-up main menu (filled black boxes) and some sub-options discussed in the text.  
 584 **(b)** Main display in *GEOCARB\_NET*. Icehouses are indicated with blue vertical shading with peak  
 585 icehouse conditions in darker blue. The lower graphic panel shows modelled CO<sub>2</sub> with errors-bars, CO<sub>2</sub>  
 586 proxies and a blue line indicating the glacial inception CO<sub>2</sub> threshold with time. The upper graphic  
 587 panel displays modelled O<sub>2</sub>, or temperatures as shown here. Five panels are shown below the main  
 588 menu: **(i) RUN MODEL:** Estimate CO<sub>2</sub> and O<sub>2</sub> with '*error analysis*' and '*refresh chart*' tick boxes. **(ii)**  
 589 **CLIMATE SENSITIVITY:** Defaults to 3° (greenhouse) and 6° (Icehouse) per doubling of CO<sub>2</sub>. If the '*glacial*  
 590 *inception threshold*' box is ticked it will draw the blue line in the CO<sub>2</sub> panel with a selected climate  
 591 sensitivity for icehouse conditions (defaults to 6°). Parameters in *GEOCARB\_NET* are averaged in 10  
 592 Myr bins and during the late Paleozoic ice age (330-260 Ma) and the end Cenozoic ice age (30-0 Ma)  
 593 climate sensitivity defaults to 6°. To simulate the Hirnantian glaciation at 445 Ma, one can select to  
 594 impose icehouse climate sensitivities at 450 and 440 Ma although this glacial event may have been  
 595 shorter than one million years (Cocks & Torsvik 2021). **(iii) CHART SETTINGS:** Adjust CO<sub>2</sub> axis (ppm)  
 596 and age range (maximum 570 Ma) and select to plot modelled O<sub>2</sub> or temperatures (SST=Sea Surface

597 Temperatures; GAT=Global Average Temperatures). **(iv) MODELS:** Toggle on/off GEOCARB\_NET  
 598 model results and various pre-calculated library models: GEOCARB (M21) = [Marcilly et al. 2021](#),  
 599 Model 12; GEOCARB (R14) = [Royer et al. \(2014\)](#); SCION = [Mills et al. \(2022\)](#), COPSE = [Lenton et](#)  
 600 [al. \(2019\)](#); COPSE-H = A hybrid model based on [Lenton et al. \(2019\)](#), GEOCLIM = [Godderis &](#)  
 601 [Donnadieu \(2019\)](#). **(v) PROXIES:** Toggle on/off different CO<sub>2</sub> proxy types, a running mean (binned)  
 602 proxy curve developed here ([Section 7](#)) and a LOESS fitted mean curve ([Foster et al. 2017](#)).

603 **FIGURE 4.** **(a)** Comparison of percentage error estimates in GEOCARB\_NET with the original ‘inner’  
 604 (red lines) and ‘outer’ (red stippled) confidence envelope (Monte Carlo Estimates) reported in [Royer et](#)  
 605 [al. \(2014\)](#). The cumulative effect of assigning a 4% uncertainty of all the variables in panel b reproduce  
 606 the ‘inner’ band Monte Carlo simulations. We also show the [Royer et al. \(2014\)](#) model run with 10%  
 607 errors. This model can be selected in ‘Restore System’ in the main ‘Organize’ menu ([Fig. 3a](#)). **(b)** The  
 608 percentage error analysis menu in GEOCARB\_NET. Time-dependent parameters ending with ‘\_G’ are  
 609 the ‘Godderis’ parameters refined in [Royer et al. \(2014\)](#). By default, all boxes are ticked but the operator  
 610 can select specific parameters to test how sensitive they are to the error analysis. Assigning an error  
 611 larger than 10% will commonly lead to model failure.

612 **Figure 5.** **(a)** Simplified carbon-cycle with depicted main sources (red colors) and sinks (blue). Carbon  
 613 sources include magmatic-related degassing from mid-ocean (MOR) ridges (1), island/continental  
 614 arcs (2, including metamorphic decarbonation), continental rifts (3) and plume-related hotspots (4, OIB). Weathering is controlled by solar forcing, paleogeography, and geomorphological factors such  
 615 as sea level, topography, lithology, and vegetation changes. Chemical weathering of silicates (5) sequesters atmospheric CO<sub>2</sub>, providing alkalinity and dissolved cations to the oceans, which promotes  
 616 calcium carbonate (CaCO<sub>3</sub>) formation. Moreover, the supply of phosphorus (P) nutrients and reactive  
 617 Fe causes enhanced burial of organic carbon. Combined, these effects lower atmospheric CO<sub>2</sub> on  
 618 different timescales. Weathering can be enhanced by extensive blankets of LIP-lava or exhumation of  
 619 ophiolites (6). Continental silicate weathering dominates over the seafloor weathering buffer  
 620 (reactions between basalt and seawater circulating through the upper oceanic crust), but the latter have  
 621 been an important carbon sink in deep time. **(b)** A Carboniferous (330 Ma) equatorially centred full  
 622 plate reconstruction with exposed land (continental crust). Exposed rocks in warm and wet  
 623 environments weather fastest, mostly within a band of 10° from the equator (pink-shaded region), and  
 624 the fraction of exposed land undergoing chemical weathering ( $f_{AW}/f_A$ ) can be approximated by the  
 625 amount of exposed land within this equatorial band ([Marcilly et al. 2021](#)) assuming similar climate  
 626 gradients as today. Conversely,  $f_{SR}$  can be estimated from seafloor production rate/subduction flux  
 627 (1/2) from full-plate models. The model shown here (and in ‘Maps’; [Figs. 3a, 7](#)) with exposed land  
 628 is refined from [Domeier & Torsvik \(2014\)](#), [Torsvik & Cocks \(2017\)](#) and [Marcilly et al. \(2021\)](#).

631

632 **Figure 6.** (a) Predicted CO<sub>2</sub> levels using different estimates for *plate tectonic degassing* ( $f_{SR}$ ). The base  
 633 model is that of [Marcilly et al. \(2021, Model 12\)](#), a hybrid model with pink shaded error estimates ( $\pm$   
 634 4%) using subduction flux (0-350 Ma) and scaled arc-zircon frequency before that time. The hybrid age  
 635 transition is shown by the yellow dot in both panels. This base model is compared with a model based  
 636 exclusively on subduction flux calculated from the full-plate model of [Merdith et al. \(2021\)](#) (blue line  
 637 with light, blue-shaded error estimates). (b) Subduction flux ( $f_{SR}$ ) relative today (=1) based on the hybrid  
 638 model of [Marcilly et al. \(2021\)](#) and the full-plate model of [Merdith et al. \(2021\)](#). To use the latter to  
 639 estimate CO<sub>2</sub> (panel a) select ‘*Change Entire Columns*’ in ‘*Edit*’ & ‘*Time-series*’ ([Fig. 3a](#)) and choose  
 640 ‘*Replace fSR (plate tectonic degassing)*’ with ‘*Subduction Flux Calculated from Merdith et al. (2021)*  
 641 *model*’.

642 **Figure 7.** Example of the ‘*Map*’ option ([Fig. 3a](#)) that shows a Pangea reconstruction at 230 Ma with  
 643 total exposed land (controls  $f_A$ ) and the distribution of climate sensitive facies such as evaporites, coal  
 644 and bauxites. Note lack of coal and bauxites in the interior of Pangea, which appear arid due to evaporite  
 645 occurrences. Thick, red-stippled lines define 10°S and 10°N, and the fainter grey lines represent the  
 646 tropical boundaries ( $\pm 23.5^\circ$ ) as defined by the Earth’s current tilt. Indicated temperature and  
 647 atmospheric CO<sub>2</sub> levels based on global average temperatures ([Scotese et al. 2021](#)) and modelled CO<sub>2</sub>  
 648 ([Marcilly et al. 2021](#), Model 12 refined). In the Triassic, East Asian (e.g., North/South China, NC/SC)  
 649 and many other Asian/Tibetan blocks were not part of Pangea and separated by the Neotethys that  
 650 opened in the early Permian.

651 **Figure 8.** (a) Testing predicted CO<sub>2</sub> levels based on our exposed tropical land estimates ( $\pm 10^\circ$ ) with  
 652 arid corrections on three different plate reconstructions. We use exposed land based on a refined model  
 653 of [Marcilly et al. \(2021\)](#) and reconstructed the distribution of exposed on the maps of [Merdith et al.  
 654 \(2021\)](#) and [Scotese \(2019\)](#). (b) In ‘*Edit*’, ‘*Time Series*’ and ‘*Change Entire columns*’, we can change  
 655  $f_{AW}/f_A$  by selecting ‘*Replace f<sub>AW</sub>/f<sub>A</sub>\_G (land area undergoing chemical weathering)*’. In panel a, we  
 656 show four different CO<sub>2</sub> curves by selecting the options marked by a red star. (c) Land area ( $\pm 10^\circ$ )  
 657 undergoing chemical weathering relative today ( $f_{AW}/f_A$ ) as indicated in panel b.

658 **Figure 9.** (a) Predicted CO<sub>2</sub> levels by replacing the land mean surface temperature curve in [Royer et  
 659 al. \(2014, ‘Godderis’\)](#) with the original GEOG curve of [Berner \(2004\)](#). We also show the effect of not  
 660 changing GEOG (= 0). (b) Comparison of the new (‘Godderis’) and old (‘Berner’) GEOG curves  
 661 (described in [Royer et al. 2014](#)). (c) In ‘*Edit*’, ‘*Time Series*’ and ‘*Change Entire columns*’, select ‘*Set  
 662 one or several time-series values to present-day*’ ([Fig. 3a](#)) and then click on the time-series that should  
 663 not change with time. In this case GEOG is set to zero for all times. Click ‘*Make changes and Exit*’,  
 664 save changes when leaving ‘*Time-series*’ menu and then ‘*Run Model*’ in main menu. That will result in  
 665 the red-stippled curve in panel a ([Marcilly et al. 2021](#), Model 12).

666 **Figure 10.** **(a)** Predicted changes in CO<sub>2</sub> by varying three plant-assisted weathering parameters (LIFE,  
 667 GYM and FERT). Changing these parameters within the quoted  $2\sigma$  values can have dramatic effects on  
 668 predicted CO<sub>2</sub> levels during the early Palaeozoic (LIFE) and the early-mid Mesozoic (GYM). **(b)** This  
 669 menu is selected in ‘Edit’ and ‘Constants’. Change the value of one or several parameters. In ‘Organize’  
 670 select ‘Save changes (and Exit)’ and the ‘Run Model’.

671 **Figure 11.** Predicted changes in CO<sub>2</sub> by varying climate sensitivity (parameters deltaT2X and GLAC).  
 672 GEOCARB is traditionally run with a climate sensitive of 3° (greenhouse) and 6° (icehouse) per  
 673 doubling of CO<sub>2</sub> (deltaT2X=3, GLAC=2). In GEOCARB\_NET we also allow the end-Ordovician  
 674 (Hirnantian) to be simulated under icehouse conditions (thick grey curve with error envelope). We also  
 675 show the effect of running GEOCARB\_NET with constant climate sensitivity at 3 and 6° (curves 2 and  
 676 3). */describe better two lower diagrams /remark on red line CS3 and the two panels below the diagram*

677 **Figure 12** **(a)** Cenozoic time scale and estimated atmospheric CO<sub>2</sub> from proxies ([The CenCO2PIP Consortium 2023](#)), shown as a black median curve with 50 and 95% credible intervals (dark and light-blue shading). The vertical dashed line represents the start of continent-wide glaciation in Antarctica and the onset of the End Cenozoic Ice Age (ECIA). The blue stippled line in both panels is the estimated CO<sub>2</sub> thresholds for glacial inception, assuming a climate sensitivity estimate of ~6°C per doubling of CO<sub>2</sub> with land ice (Royer 2006) and a fainter sun in the past. The estimated CO<sub>2</sub> threshold at the start of the ECIA is ~530 ppm. **(b)** Binned average CO<sub>2</sub> proxy curve (10 Myr bins) implemented in GEOCARB\_NET (see text). Mean values without 95% standard error bars (unless N=1). The modelled curve is a refined version of [Marcilly et al. \(2021\)](#) model 12 and with the ‘Hirnantian’ climate sensitivity option ([Section 6](#)). **(c)** Binned ‘tropical’ ( $\pm 30^\circ$ ) sea surface temperatures (SSTs) and individual temperature estimates (blue circles). We also show a global average temperature (GAT; [Scotese et al. 2021](#)) curve. Note the large differences from the Ordovician to the early Carboniferous and the Hirnantian sharp dip in temperature has been exaggerated (ad hoc correction). Note the logarithmic CO<sub>2</sub> scale in panels **a-b**.

691 **Figure 13.** **(a)** Predicted changes in atmospheric O<sub>2</sub> if the default δ<sup>13</sup>C<sub>carb</sub> time-series is replaced with  
 692 the δ<sup>13</sup>C record of Cramer & Jarvis (2020). The δ<sup>13</sup>C<sub>carb</sub> record was strongly smoothed using a Savitzky-  
 693 Golay filter to avoid model failure ([Appendix 1](#)) and the most notably changes are seen during the LPIA  
 694 (up to ~20%). Revised δ<sup>13</sup>C<sub>carb</sub> mean values found in ‘Isotope\_Time\_Series\_2023.csv’ ('/System'  
 695 directory). In ‘Edit’ ‘Time-Series’ ([Fig. 3a](#)) select ‘Change Entire Columns’ and ‘Update d13C’ to test  
 696 changes to your model. **(b)** GEOCARB\_NET model, i.e., [Marcilly et al. \(2021, Model 12\)](#) with refined  
 697 weathering parametrization back to 540 Ma and run with a 4% error band (dark grey envelope) and  
 698 compared with the maximum spread (variance) in predicted CO<sub>2</sub> levels from all our examples ([Figs. 6,](#)  
 699 [8-11](#)). The most important parameters causing these variances at some selected times are listed in  
 700 decreasing importance, and include land-assisted weathering parameters (LIFE, GYM), climate

701 sensitivity (CS), fraction of exposed land undergoing chemical weathering ( $f_{\text{AW}}/f_{\text{A}}$ ), change in the mean  
702 land-surface temperature undergoing chemical weathering (GEOG) and '*plate tectonic*' degassing ( $f_{\text{SR}}$ ).  
703 We also show predicted CO<sub>2</sub> levels (red line) after changes in the  $\delta^{13}\text{C}_{\text{carb}}$  time series (panel a). Both  
704 models are compared with a running mean CO<sub>2</sub> proxy curve (10 Myr bins) for the past 450 Myrs with  
705 95% standard error confidence error bars ([Section 6](#)). **(c)** The effect of running COPSE ([Lenton et al.](#)  
706 [2019](#)) with climate sensitivity (3°/6° during greenhouses/icehouses) and plate tectonic degassing and  
707 weathering parametrization as in [Marcilly et al. \(2021, Model 12\)](#) for the past 520 Myrs. In both models  
708 we used a climate sensitivity of 6° across the Hirnantian (see text). After changes in the parametrization,  
709 COPSE shows a strong positive correlation with GEOCARB\_NET (Pearson r-correlation=0.87) and  
710 predicted CO<sub>2</sub> levels during icehouses are close to or below the threshold for glacial inception (blue  
711 stippled line; assumes a climate sensitivity of 6° for icehouses).

## FIGURES

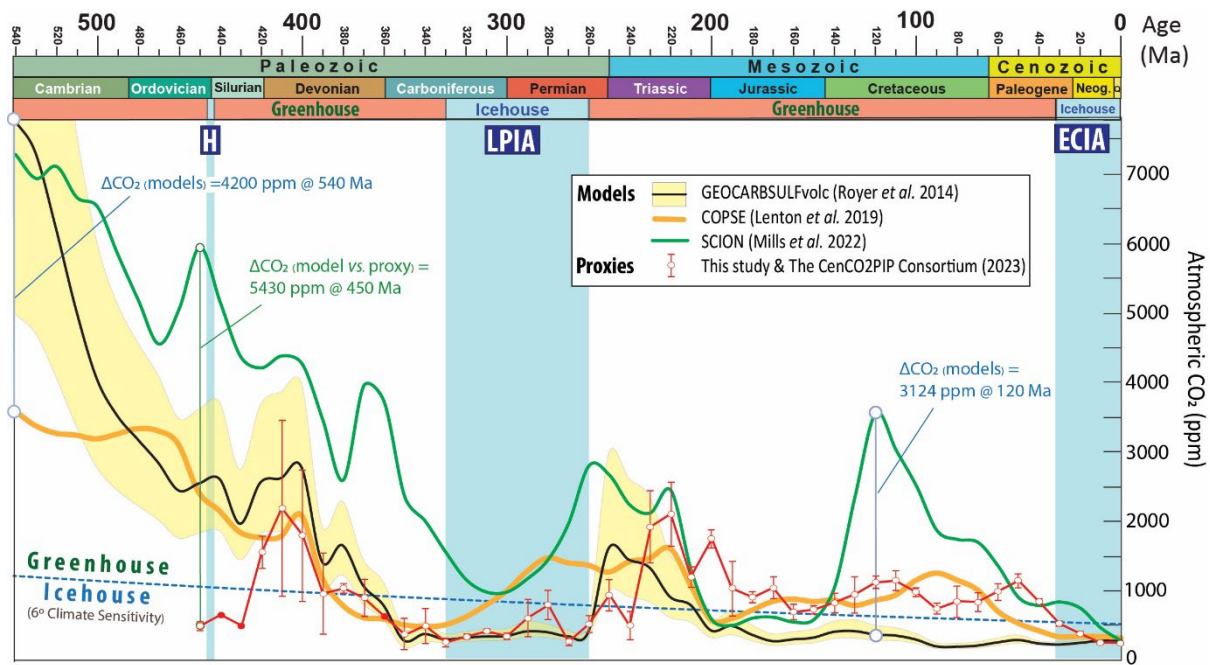


Figure 1.

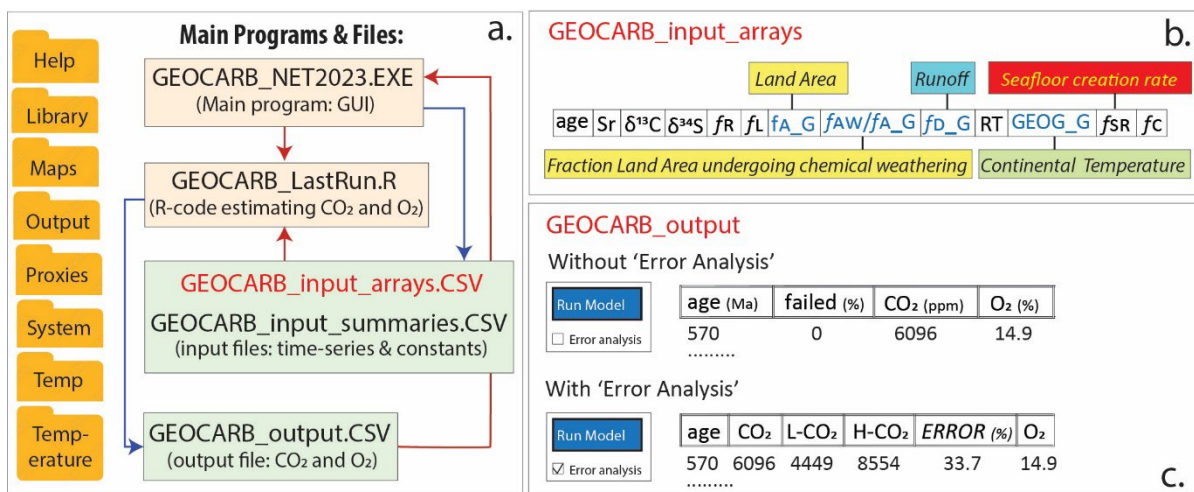


FIGURE 2.



**FIGURE 3.**

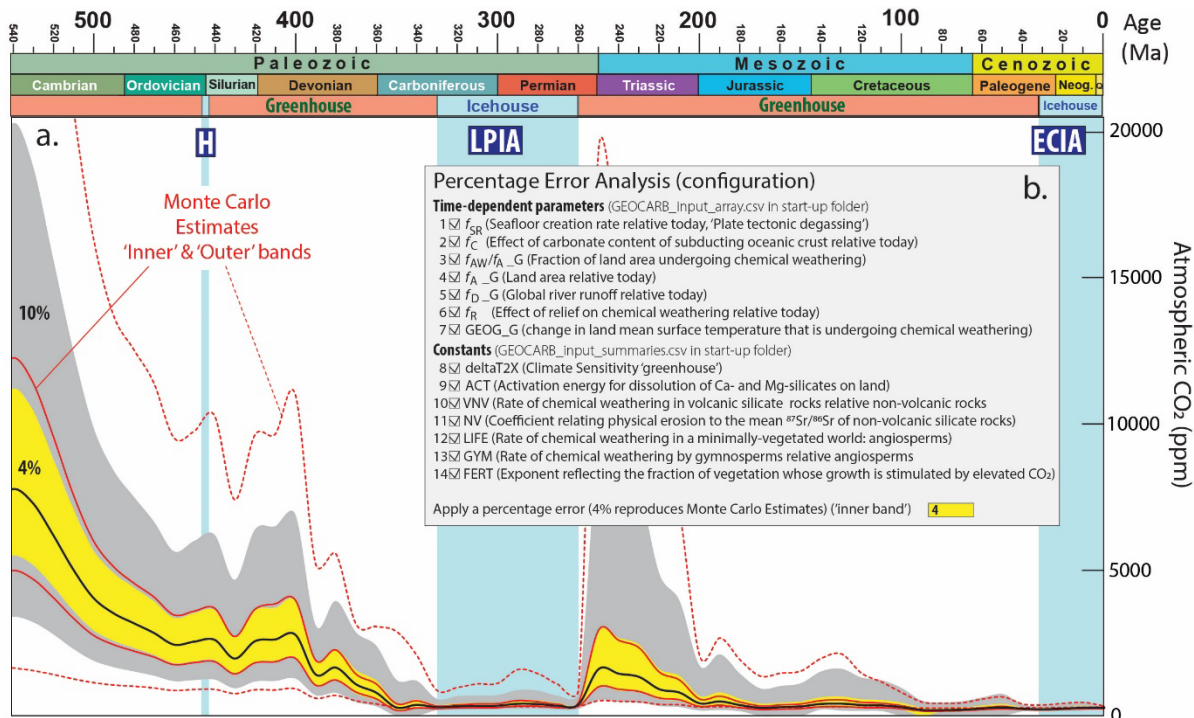


FIGURE 4.

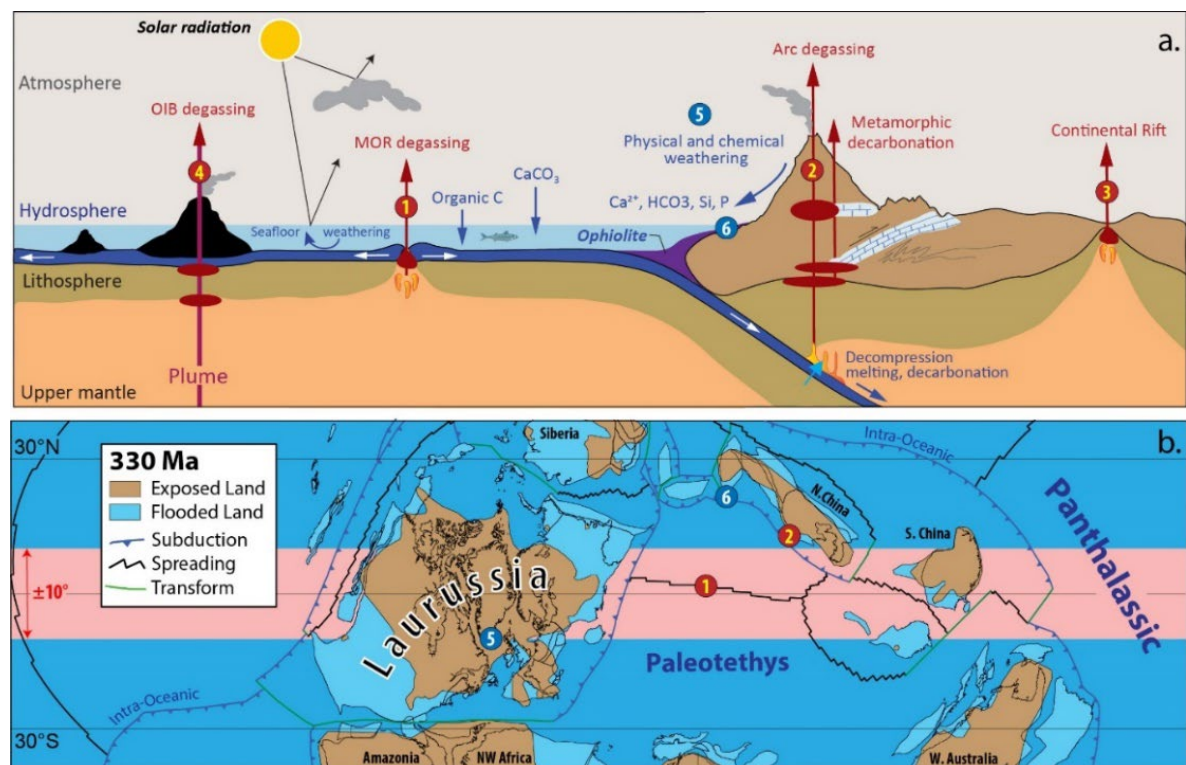
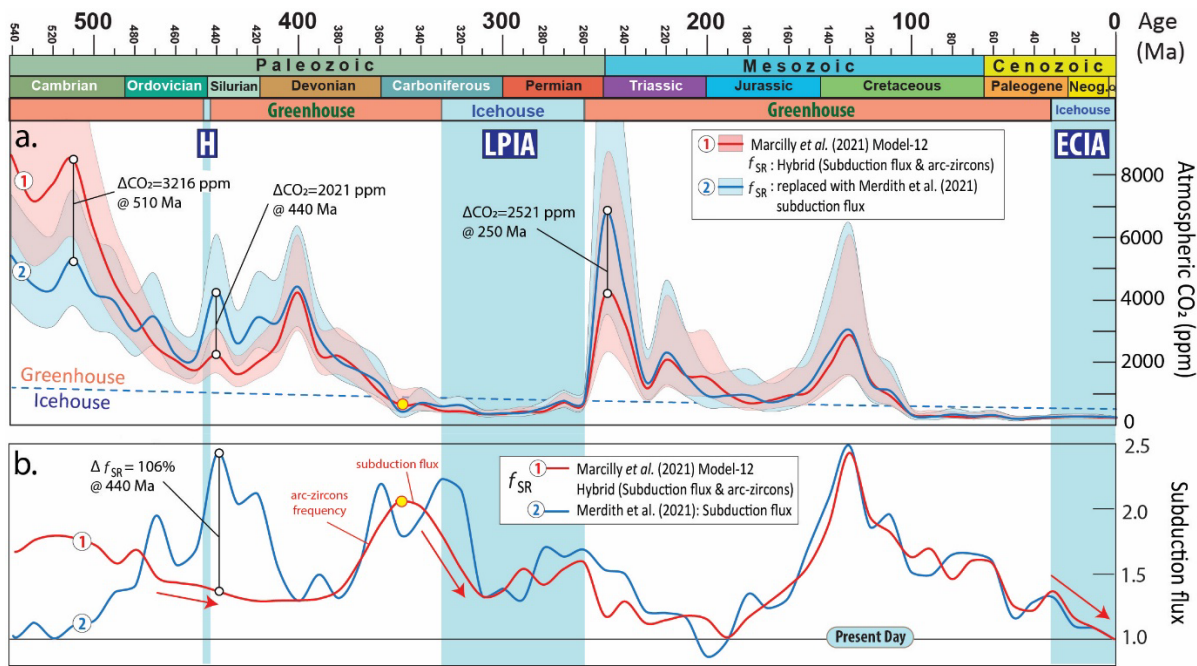
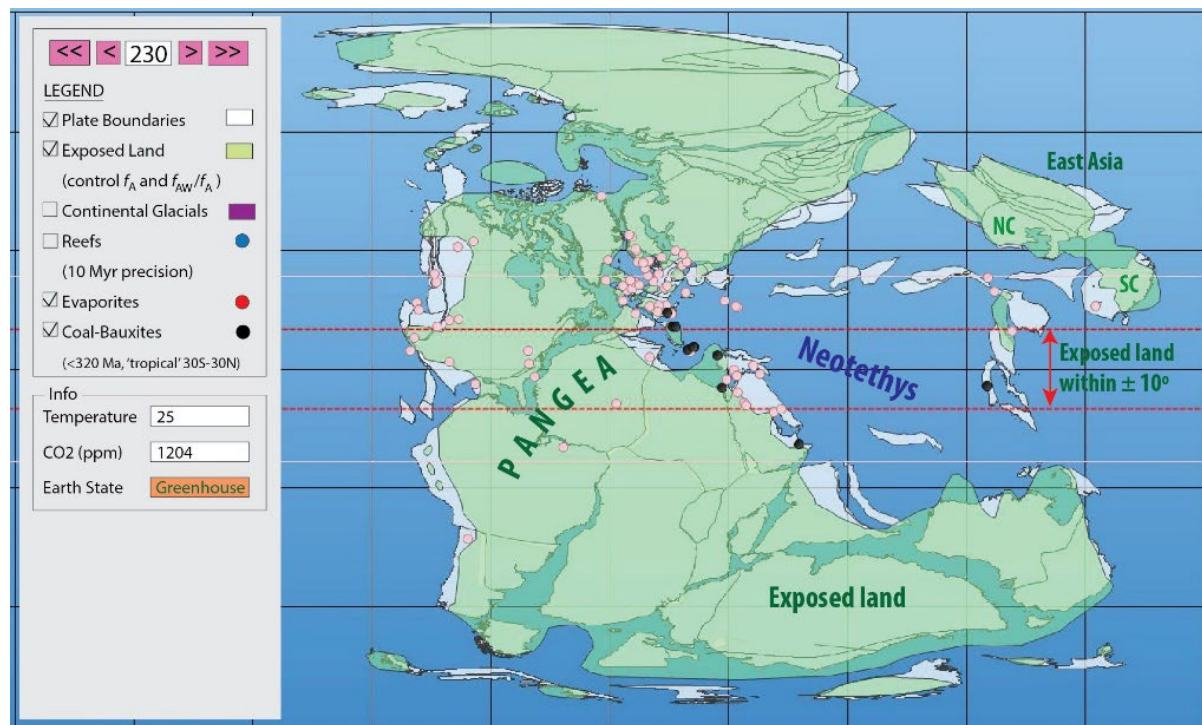
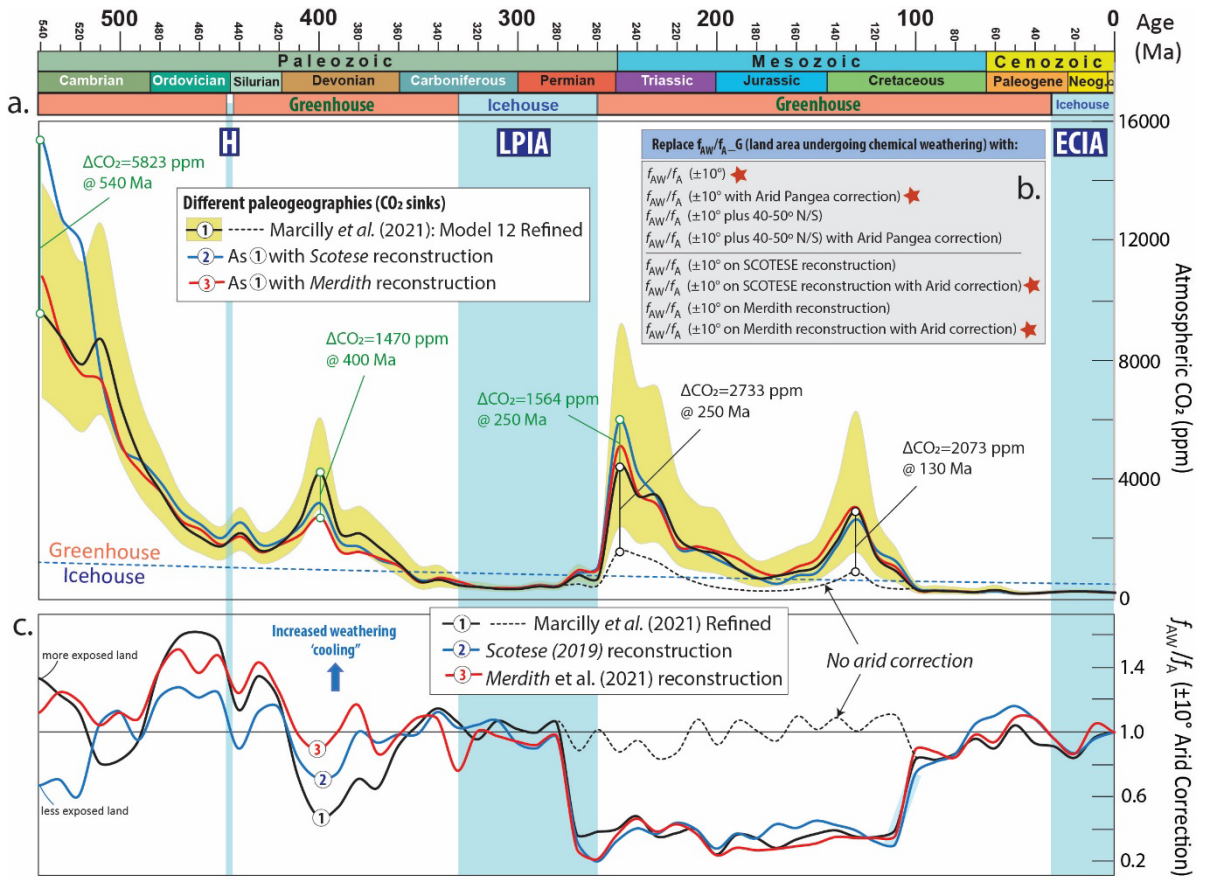


FIGURE 5



**FIGURE 6.**





**FIGURE 8.**

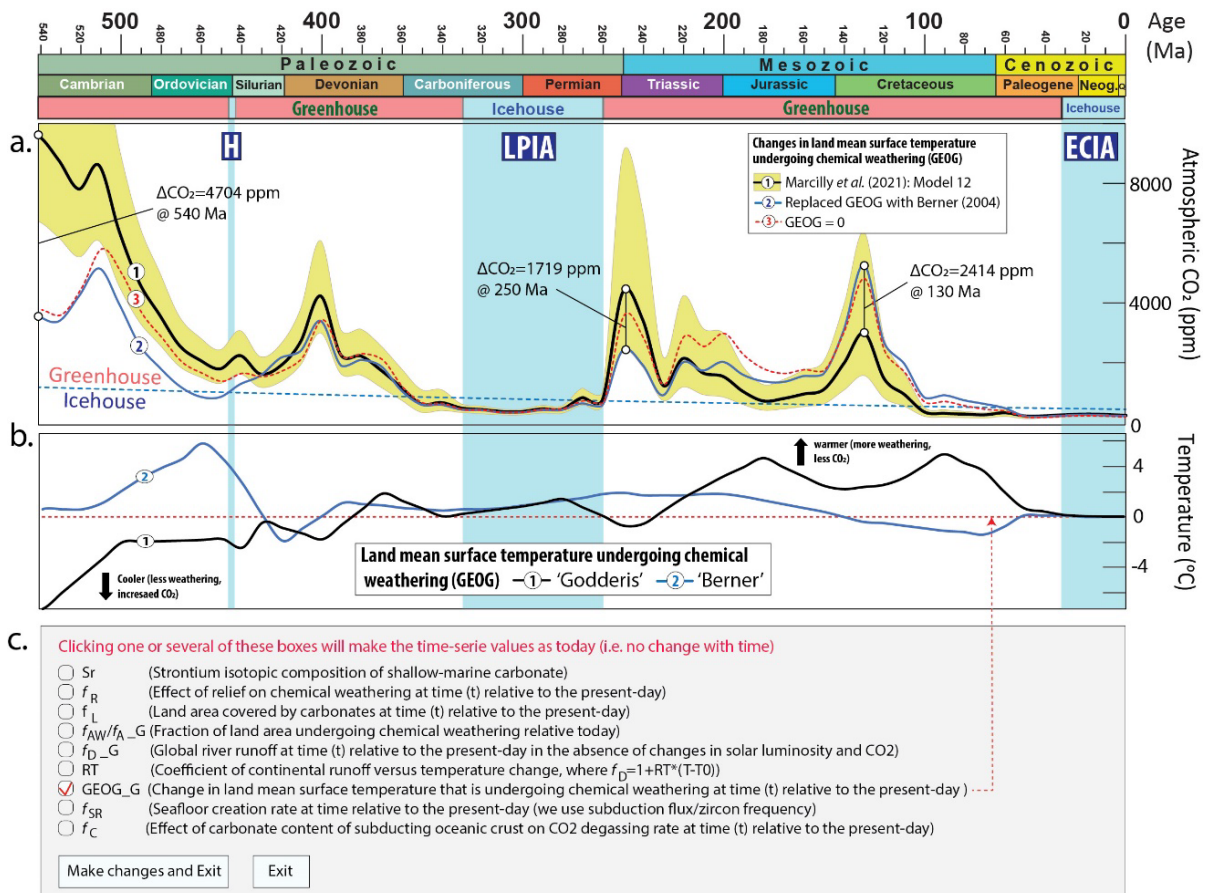


**FIGURE 9.**

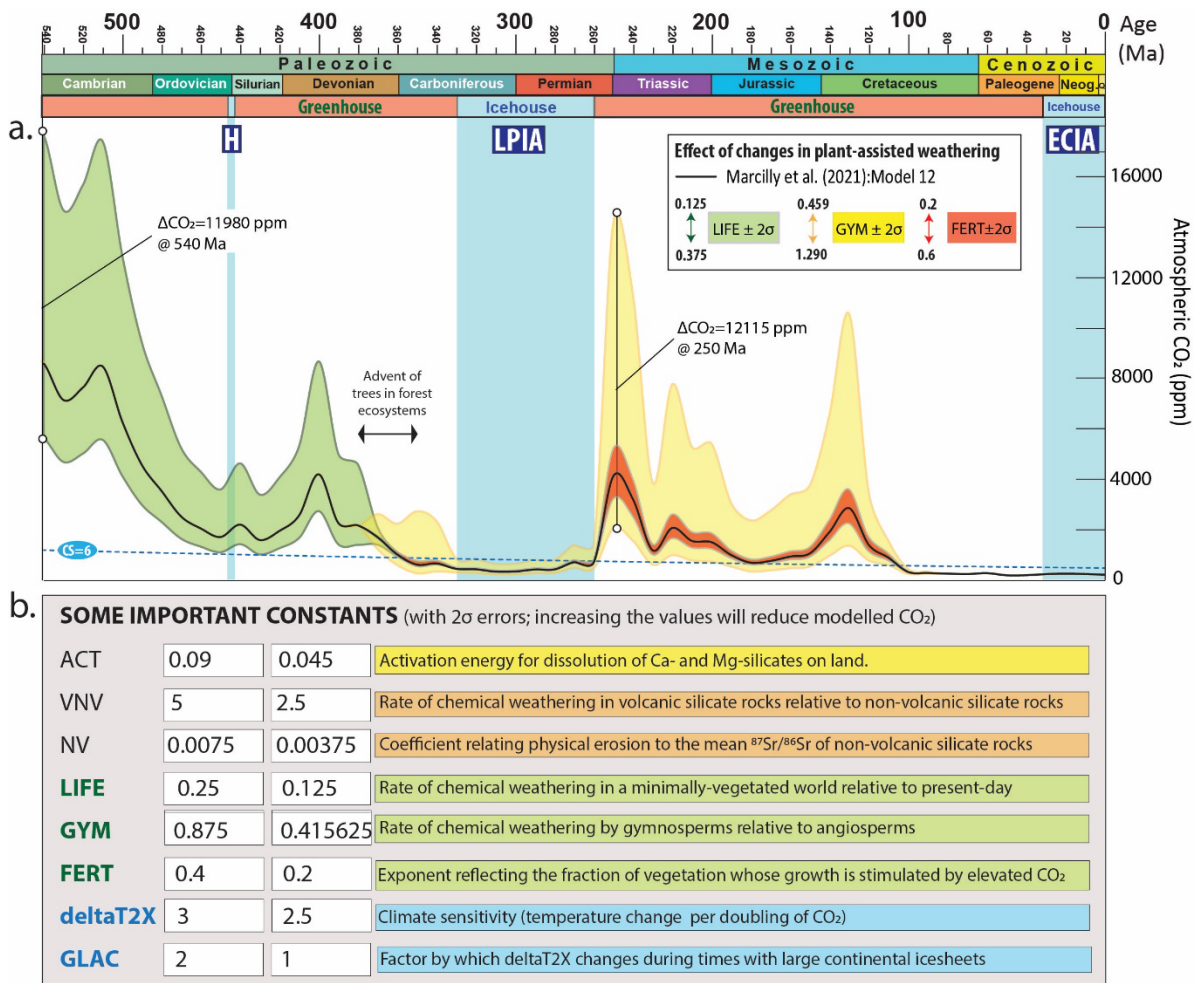


**FIGURE 10.**

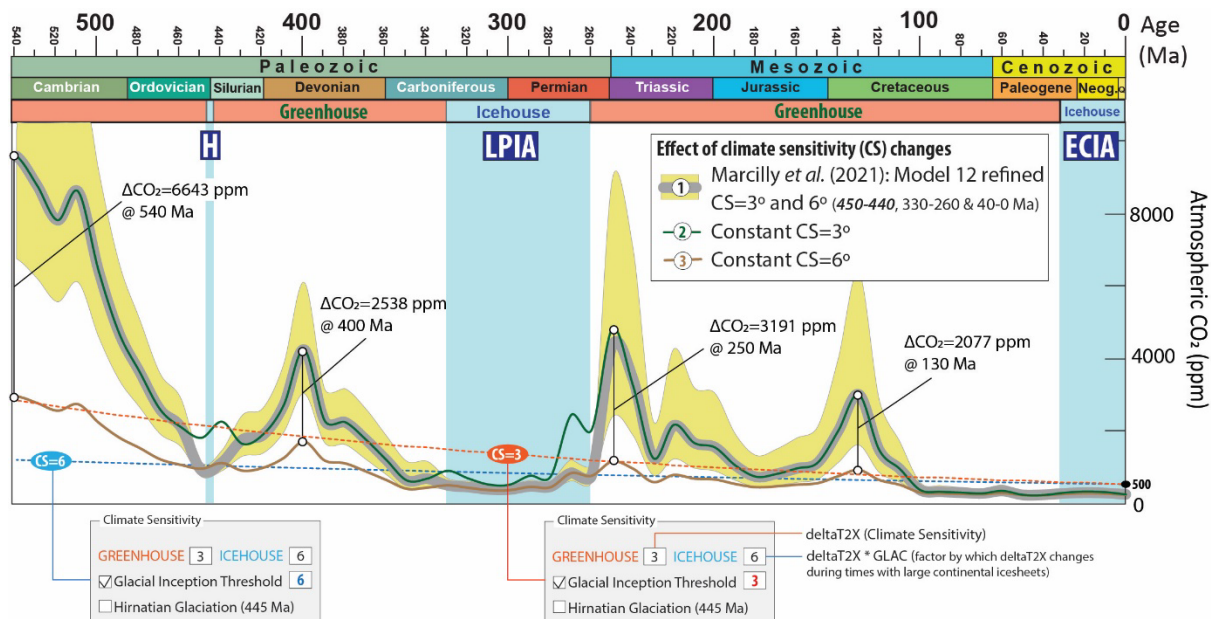


**FIGURE 11**

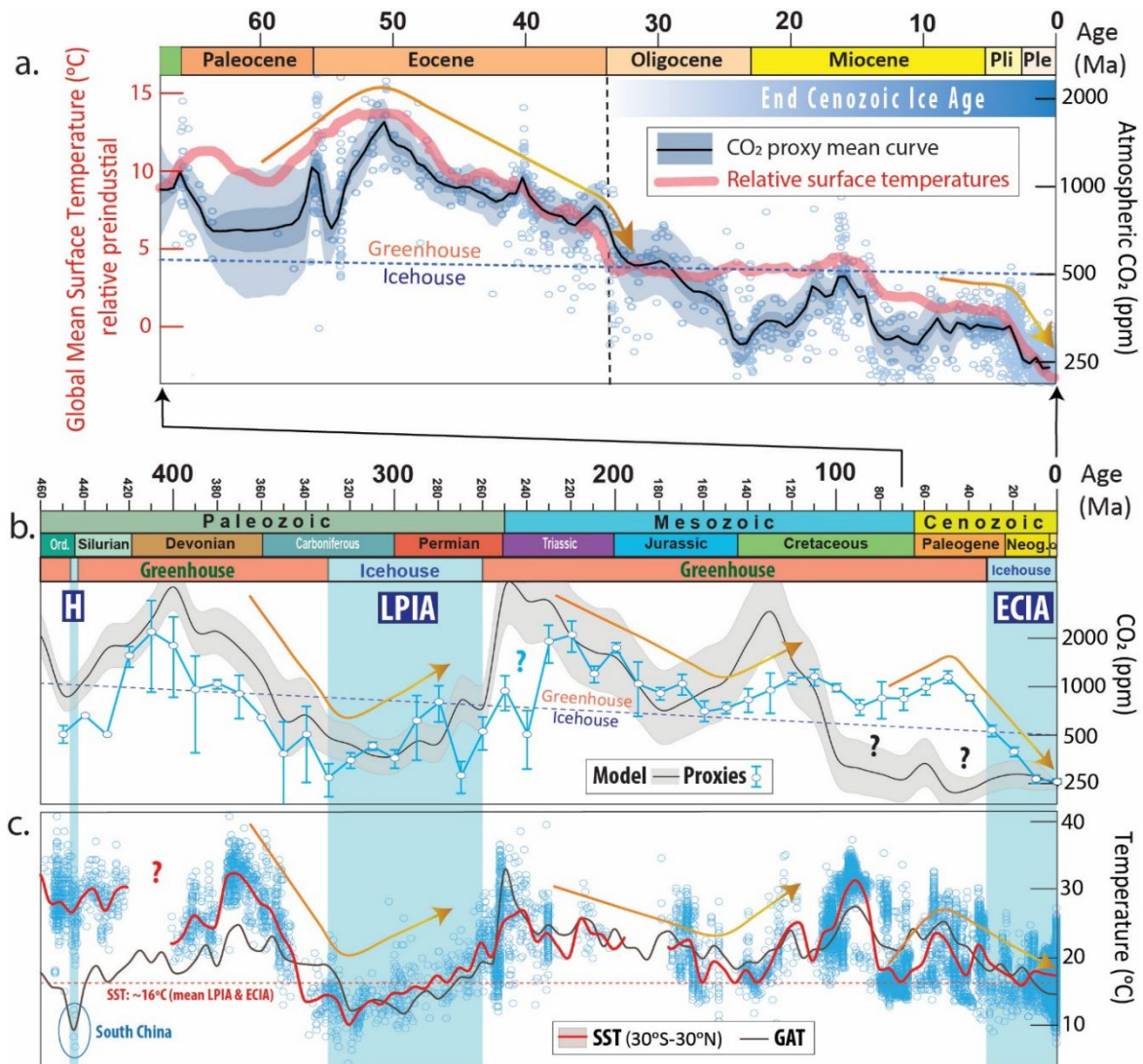


**FIGURE 12**

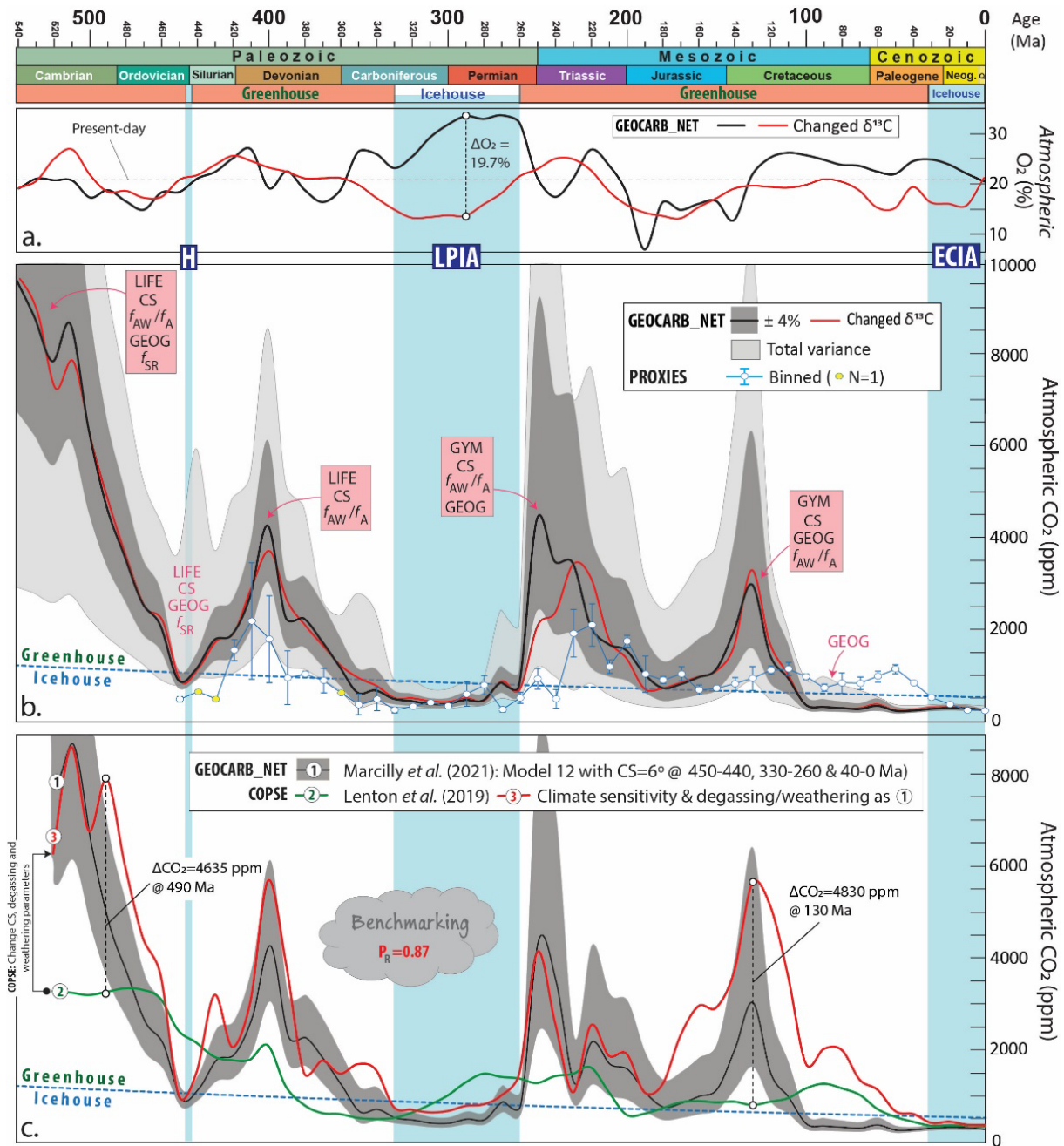


**FIGURE 13**